JCB Journal of Cell Biology

ARTICLE

MASTL promotes cell contractility and motility through kinase-independent signaling

Maria Emilia Taskinen[1]*, Elisa Närvä[1]*, James R.W. Conway[1], Laura Soto Hinojosa[2], Sergio Lilla[3], Anja Mai[1], Nicola De Franceschi[1], Laura L. Elo[1], Robert Grosse[2], Sara Zanivan[3,4], Jim C. Norman[3,4], and Johanna Ivaska[1,5]

Microtubule-associated serine/threonine-protein kinase-like (MASTL) is a mitosis-accelerating kinase with emerging roles in cancer progression. However, possible cell cycle–independent mechanisms behind its oncogenicity remain ambiguous. Here, we identify MASTL as an activator of cell contractility and MRTF-A/SRF (myocardin-related transcription factor A/serum response factor) signaling. Depletion of MASTL increased cell spreading while reducing contractile actin stress fibers in normal and breast cancer cells and strongly impairing breast cancer cell motility and invasion. Transcriptome and proteome profiling revealed MASTL-regulated genes implicated in cell movement and actomyosin contraction, including Rho guanine nucleotide exchange factor 2 (GEF-H1, *ARHGEF2*) and MRTF-A target genes tropomyosin 4.2 (*TPM4*), vinculin (*VCL*), and nonmuscle myosin IIB (NM-2B, *MYH10*). Mechanistically, MASTL associated with MRTF-A and increased its nuclear retention and transcriptional activity. Importantly, MASTL kinase activity was not required for regulation of cell spreading or MRTF-A/SRF transcriptional activity. Taken together, we present a previously unknown kinase-independent role for MASTL as a regulator of cell adhesion, contractility, and MRTF-A/SRF activity.

Downloaded from http://rupress.org/jcb/article-pdf/219/6/e201906204/1615651/jcb_201906204.pdf by guest on 09 February 2026

Introduction

Microtubule-associated serine/threonine-protein kinase-like (MASTL, also known as Greatwall kinase) has emerged as a putative oncogene that is highly expressed in several cancers (Marzec and Burgess, 2018). In breast cancer, MASTL expression increases with advanced clinical stage and predicts poor survival (Álvarez-Fernández et al., 2018; Rogers et al., 2018; Wang et al., 2016; Yoon et al., 2018), with high MASTL levels positively correlating with increased tumor growth and metastasis in vivo (Álvarez-Fernández et al., 2018; Rogers et al., 2018; Vera et al., 2015). Moreover, knockdown of MASTL induces radiosensitivity (Nagel et al., 2015), which makes MASTL an appealing pharmacological target. However, the exact mechanism of how MASTL facilitates tumorigenicity remains unknown. Interestingly, while kinase inhibitors of MASTL are under development as potential drugs for cancer therapy (Ammarah et al., 2018), the role of MASTL kinase activity remains unclear in relation to its oncogenic properties.

Cell adhesion plays a critical role in cancer progression and metastasis (Hamidi and Ivaska, 2018), where serine/threonine kinases are important regulators of adhesion and contraction (Zaidel-Bar et al., 2015). MASTL has an established role in the acceleration of cell cycle progression through phosphorylation of Endosulfine Alpha (ENSA) and Arpp19, which inhibit PP2A-B55 phosphatase activity and thus maintain the phosphorylation of CDK1 substrates (Vigneron et al., 2016). However, recent studies suggest that MASTL has additional roles besides cell cycle regulation, such as during DNA replication (Charrasse et al., 2017), recovery from DNA damage (Wong et al., 2016), and regulation of epithelial cell contact inhibition (Rogers et al., 2018). Here, we demonstrate a kinase-activity independent role for MASTL in governing/restraining cell spreading and attachment to the ECM in mammary epithelial and breast cancer cells. Mechanistically, MASTL regulates serum response factor (SRF)/myocardin-related transcription factor (MRTF)–mediated transcription in a kinase-independent manner through associating with MRTF-A and supporting its nuclear retention. MASTL induces cell contractility and cell migration by supporting the expression of several proteins, including Rho guanine nucleotide exchange factor 2 (GEF-H1) and the SRF/MRTF target genes tropomyosin 4.2 (Tpm4.2), nonmuscle myosin IIB (NM-2B), and vinculin (VCL).

---

[1]Turku Bioscience Centre, University of Turku and Åbo Akademi University, Turku, Finland; [2]Institute of Experimental and Clinical Pharmacology and Toxicology, University of Freiburg, and Center for Integrative Biological Signalling Studies, Freiburg, Germany; [3]Cancer Research UK Beatson Institute, Glasgow, UK; [4]Institute of Cancer Sciences, University of Glasgow, Glasgow, UK; [5]Department of Biochemistry, University of Turku, Turku, Finland.

*M.E. Taskinen and E. Närvä contributed equally to this paper; Correspondence to Johanna Ivaska: johanna.ivaska@utu.fi.

© 2020 Taskinen et al. This article is distributed under the terms of an Attribution–Noncommercial–Share Alike–No Mirror Sites license for the first six months after the publication date (see http://www.rupress.org/terms/). After six months it is available under a Creative Commons License (Attribution–Noncommercial–Share Alike 4.0 International license, as described at https://creativecommons.org/licenses/by-nc-sa/4.0/).

Rockefeller University Press
J. Cell Biol. 2020 Vol. 219 No. 6 e201906204
https://doi.org/10.1083/jcb.201906204

Check for updates

Results

MASTL inhibits cell spreading and attachment

To investigate whether MASTL would play a role in cell adhesion, we silenced MASTL for 48 h in MDA-MB-231 breast cancer cells and imaged cell morphology following replating on collagen for 2 h. MASTL-depleted cells were significantly more spread than the control siRNA transfected cells (Fig. 1, A and B; and statistics for all experiments, Table S1). Furthermore, MASTL silencing significantly increased cell attachment (area occupied by cells on ECM) of single cells plated and monitored in real time (Fig. 1 C). Increased cell attachment after MASTL silencing was observed with two independent siRNA oligos and was similar on collagen and fibronectin (Fig. S1, A–D).

Conversely, EGFP-MASTL WT overexpression significantly reduced cell spreading compared with the EGFP control (Fig. 1, D and E; and Fig. S1 E). Expressing siRNA-resistant WT EGFP-MASTL fully reversed the increased cell spreading in MASTL-silenced breast cancer cells (Fig. 1, F–I; and Fig. S1 F). Interestingly, expression of kinase-dead MASTL (EGFP-MASTL G44S; Vera et al., 2015) was equally effective in reversing spreading of MASTL-silenced MDA-MB-231 cells (Fig. 1, G and H), indicating that MASTL regulates cell spreading independent of its kinase activity.

MASTL was expressed in normal human mammary epithelial MCF10A, luminal breast cancer MCF7, and triple-negative breast cancer MDA-MB-231 cells, with the highest expression detected in the cancer cells (Fig. S2 A). Importantly, MASTL depletion increased significantly the spreading of MCF10A (Fig. 2, A and B) and MCF7 cells (Fig. S2, B and C), indicating that this effect is not restricted to MDA-MB-231 cancer cells. Taken together, these data suggest that MASTL inhibits cell spreading and adhesion in normal and cancerous mammary epithelial cells on different ECM substrates.

MASTL regulates cell spreading independently of focal adhesion size, integrin activity, or cell cycle

To investigate the possible mechanisms of MASTL-induced inhibition of cell spreading, we studied if MASTL silencing affects focal adhesions or integrin expression/activity. MASTL silencing did not significantly influence the size of paxillin-positive focal adhesions between control and silenced cells (Fig. 2 C). However, while the significantly more spread MASTL-silenced cells displayed a larger number of focal adhesions per cell, this equated to fewer adhesions over cell area when compared with the smaller control cells (Fig. 2 D). Silencing of MASTL increased slightly, but significantly, the levels of total β1 integrin at the cell surface (Figs. 2 E and S2 D) in MDA-MB-231 cells. However, the levels of active β1 integrin (detected with the conformation specific 12G10 antibody) and overall β1 integrin activity (relative activation index) were not changed (Fig. 2, F and G; and Fig. S2, E–G). In addition, binding of MASTL-silenced cells to labeled fibronectin (FN7-10 fragment) was slightly but significantly lower than in control cells (Fig. 2 H). Thus, MASTL does not inhibit cell spreading through the regulation of integrin-ECM affinity or focal adhesion size.

Long-term silencing of MASTL has been reported to cause a delay in the G2 phase of the cell cycle (Voets and Wolthuis, 2010), whereas short-term silencing (48 h) has no effect on the cell cycle of human dermal fibroblasts, human umbilical vein endothelial cells, or MCF10A cells (Yoon et al., 2018). Similarly, we found that the cell cycle profile of MDA-MB-231 cells was unaltered after short-term (48 h, used in all of our experiments) MASTL silencing (Fig. 2 I; and Fig. S2, H and I).

Previous work has demonstrated that MASTL-overexpressing MCF10A cells fail to form a single monolayer, with cells displaying disorganized actin, E-cadherin, and β-catenin localization (Rogers et al., 2018). We found that MASTL silencing, in confluent MCF10A cells, dramatically increases cell spreading without disrupting E-cadherin or β-catenin localization to junctions or significantly affecting junction alignment (Fig. 3, A–F). However, junctions were occasionally disrupted, leaving gaps in the MASTL-silenced cell monolayer (Fig. 3, A and B).

MASTL supports expression of cell movement– and actin cytoskeleton–related genes

To obtain an unbiased view of the molecular players implicated in MASTL control of cell adhesion, we performed genome-wide transcriptome analysis in MASTL-depleted cellsFig. S3, A and B). Genes with a false discovery rate (FDR) <5% were considered as differentially expressed; this resulted in 139 and 247 altered transcripts at 24 h and 48 h after MASTL silencing, respectively (Fig. 4 A and Table S2). The changes at 24 h and 48 h were highly correlated (Pearson correlation 0.73, $P < 2.2e\text{-}16$). Interestingly, nearly 75% of all the differentially expressed transcripts were down-regulated after MASTL silencing, implying that MASTL supports mRNA levels of multiple genes. Ingenuity Pathway Analysis software (Qiagen; https://www.qiagenbioinformatics.com/products/ingenuitypathway-analysis) revealed that the major function suppressed in MASTL-depleted cells was migration and invasion (Fig. 4 B).

Next, we investigated the effect of MASTL depletion on the cellular proteome using quantitative SILAC (stable isotope labeling with amino acids in cell culture)–based mass spectrometry proteomics (Fig. S3 C). Out of 8,418 identified proteins, 52 were found to be significantly altered in all four replicates (Fig. 4 C and Table S3). In line with the transcriptome analysis, the majority of the altered proteins were down-regulated. In addition, the top function identified was cellular movement ($P = 3.24E\text{-}07$). Furthermore, more than half of the down-regulated proteins overlapped with the down-regulated mRNAs (Fig. 4 D). This suggests that MASTL regulates cell morphology via control of cell movement–related genes.

MASTL induces GEF-H1, TPM4.2, and NM-2B levels

To identify possible actin regulators that may control MASTL-dependent cell spreading and cellular movement, we compared the transcriptome and proteome of MASTL-silenced cells to the contractome, a list of 100 literature-curated proteins associated with actomyosin contraction in nonmuscle cells (Zaidel-Bar et al., 2015; Fig. 5 A). This analysis highlighted the potential role of Rho guanine nucleotide exchange factor 2 (GEF-H1, *ARHGEF2*) as a contractility regulator downstream of MASTL. GEF-H1 is one of the key regulators of actomyosin contraction and cell motility. It induces F-actin meshwork formation in lamellipodia and membrane ruffles and facilitates cell retraction

Downloaded from http://rupress.org/jcb/article-pdf/219/6/e201906204/1615651/jcb_201906204.pdf by guest on 09 February 2026

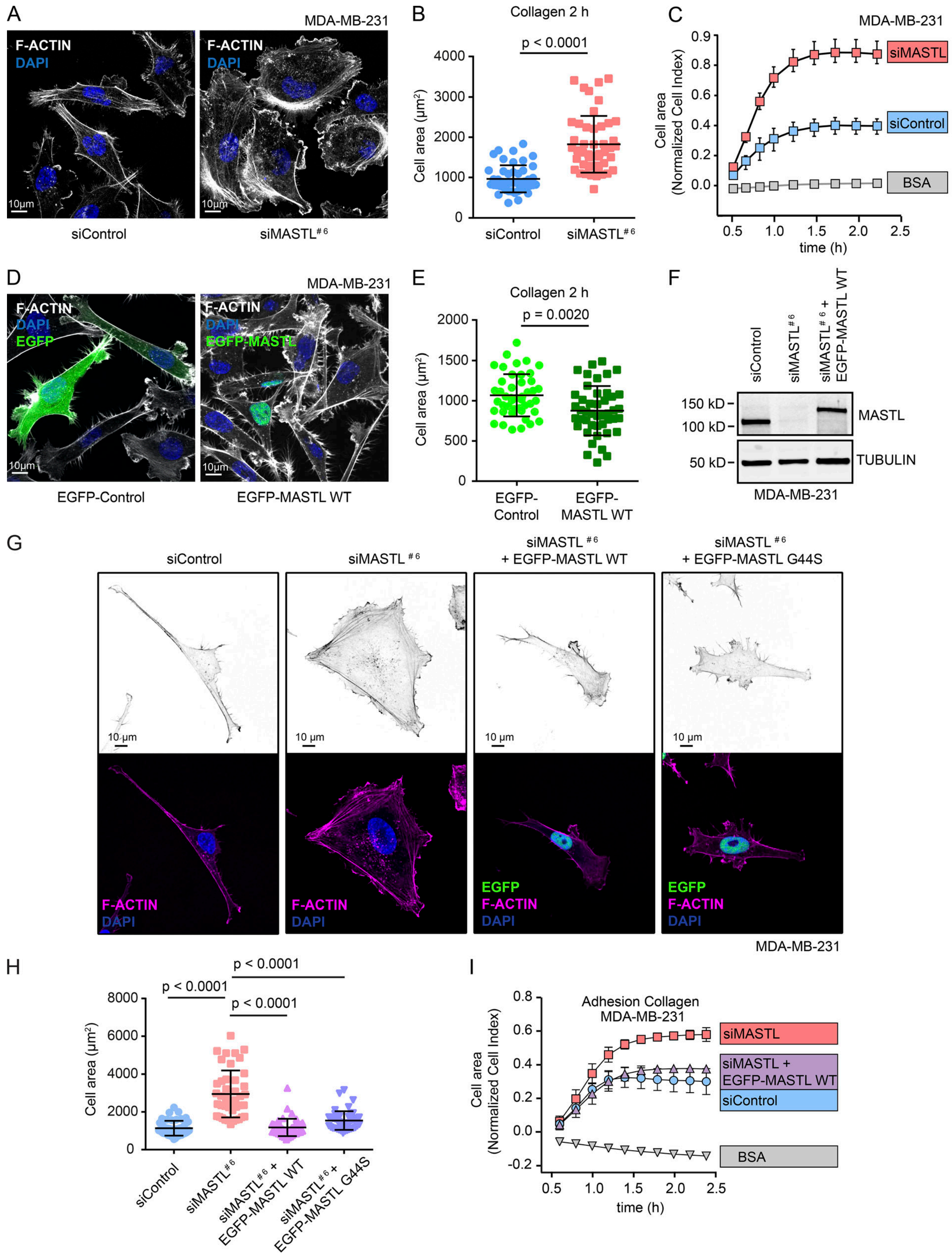

Figure 1. **MASTL inhibits cell spreading and attachment through kinase-independent functions. (A)** Representative images of F-actin (Phalloidin-Atto) and DAPI staining in control (siControl) or MASTL-silenced (siMASTL; 48-h silencing) MDA-MB-231 cells plated on collagen for 2 h. Images were acquired on a Zeiss LSM 880 Airyscan confocal. **(B)** Quantification of cell area based on F-actin staining of 45 cells (three independent experiments) from A. **(C)** Real-time monitoring of siControl or siMASTL cell area (normalized cell index) during cell spreading measured with the xCELLigence RTCA system. Single-cell suspensions were plated on collagen. BSA coating was used as a negative control. Shown are representative curves from an individual experiment. **(D)** Representative F-actin (Phalloidin-Atto) and DAPI staining in EGFP-control and EGFP-MASTL WT–overexpressing (24 h) MDA-MB-231 cells plated on collagen for 2 h. Images

Downloaded from http://rupress.org/jcb/article-pdf/219/6/e201906204/1615651/jcb_201906204.pdf by guest on 09 February 2026

were acquired on a 3i CSU-W1 spinning disk confocal. **(E)** Quantification of cell area based on the F-actin staining of 45 cells (three independent experiments) from D. **(F)** Western blot analysis of MASTL levels in siControl, siMASTL, and siMASTL + EGFP-MASTL WT (24 h MASTL silencing + 24 h expression of siRNA-resistant EGFP-MASTL WT) MDA-MB-231 cells. Tubulin was used as a loading control. **(G)** Representative images of F-actin (Phalloidin-Atto) and DAPI staining in siControl, siMASTL, siMASTL + EGFP-MASTL WT, or siMASTL + EGFP-MASTL G44S MDA-MB-231 cells plated on collagen for 2 h (3i CSU-W1 spinning disk confocal). **(H)** Quantification of cell area based on the F-actin staining of 45 cells (three independent experiments) from G. **(I)** Representative cell spreading curves and cell area (normalized cell index; as in C) of siControl, siMASTL, or siMASTL + EGFP-MASTL WT MDA-MB-231 cells. Data in all graphs are from $n = 3$ biologically independent experiments (unpaired t test, mean ± SD). See also Fig. S1 and Table S1.

---

by enhancing actin stress fiber formation (Birkenfeld et al., 2008). In addition, other contractome proteins including tropomyosin 4.2 (Tpm4.2, *TPM4*), an actin-binding protein that supports stress fiber formation and actomyosin contraction through nonmuscle myosin II ATPase activity (Gateva et al., 2017; Geeves et al., 2015; Tojkander et al., 2011), and NM-2B (*MYH10*), a nonmuscle myosin-2 isoform, were significantly down-regulated in MASTL-silenced cells.

We validated the down-regulation of *ARHGEF2* (GEF-H1), *TPM4* (Tpm4.2), and *MYH10* (NM-2B) in MASTL-silenced MDA-MB-231 cells using real-time quantitative PCR (RT-qPCR) analysis (Fig. 5 B), Western blot (Fig. 5, C–H; and Fig. S4 A) and immunofluorescence (Fig. S4 B). GEF-H1 was clearly reduced in MDA-MB-231 cells silenced with two independent siRNA oligos (Fig. 5 C; and Fig. S4, A and B) and in MCF10A cells (Fig. S4 C), suggesting that regulation of GEF-H1 is not restricted to cancer cells. Unfortunately, we were unable to detect NM-2B or Tpm4.2 in MCF10A cells consistently due to the lack of specific bands in the Western blot. However, we were able to validate Tpm4.2 reduction in MASTL-silenced confluent MCF10A cells with two independent siRNAs using immunofluorescence (Fig. S4 D). Importantly, down-regulation of GEF-H1, Tpm4.2, and NM-2B was reversed upon reexpression of siRNA-resistant EGFP-MASTL in MDA-MB-231 cells (Fig. 5 I), indicating that the down-regulation of these proteins was not due to any

Downloaded from http://rupress.org/jcb/article-pdf/219/6/e201906204/1615651/jcb_201906204.pdf by guest on 09 February 2026

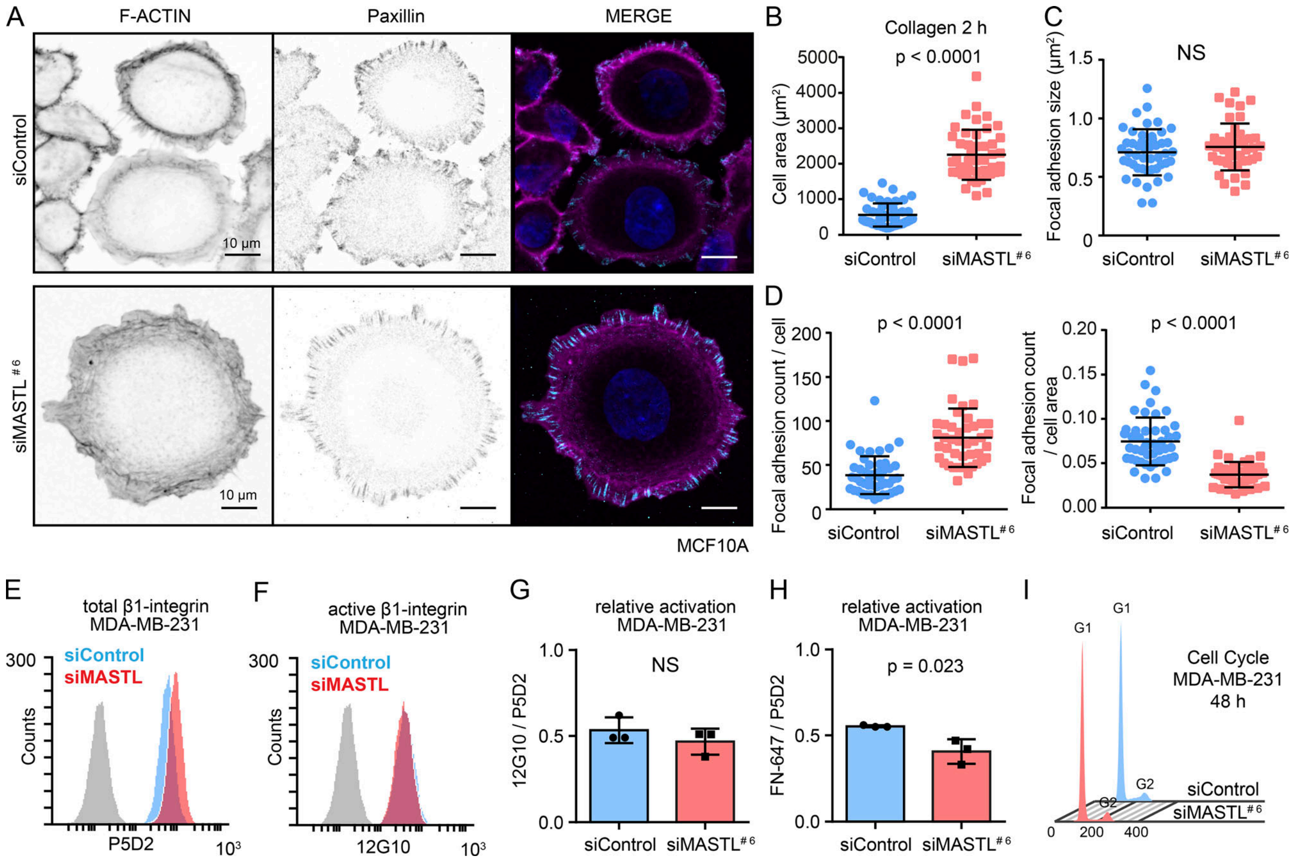

Figure 2. **MASTL regulates cell spreading independently of focal adhesion size, integrin activity, or cell cycle. (A)** Representative images of F-actin (Phalloidin-Atto), paxillin, and DAPI staining in siControl and siMASTL (48 h silencing) MCF10A cells plated on collagen for 2 h. Images were acquired on a 3i CSU-W1 spinning disk confocal. **(B–D)** Quantification of cell area based on F-actin staining, 45 cells/condition in total (B), focal adhesion size based on paxillin staining (C), and focal adhesion count based on paxillin relative to individual cells or total cell area (D), with 47 (siControl) or 44 (siMASTL) cells in total (three independent experiments) from A. **(E and F)** Representative flow cytometry histograms of total β1-integrin (P5D2; E) or active β1-integrin (12G10; F) in siControl and siMASTL MDA-MB-231 cells. **(G)** Quantification of active β1 integrin (12G10) levels relative to total β1 integrin (P5D2) from E and F. **(H)** Quantification of integrin binding to labeled fibronectin (FN-647) relative to total β1 integrin (P5D2) analyzed with flow cytometry. **(I)** Cell cycle profiles of siControl and siMASTL MDA-MB-231 cells. Data in all graphs are from $n = 3$ biologically independent experiments (unpaired t test, mean ± SD). See also Fig. S2 and Table S1.

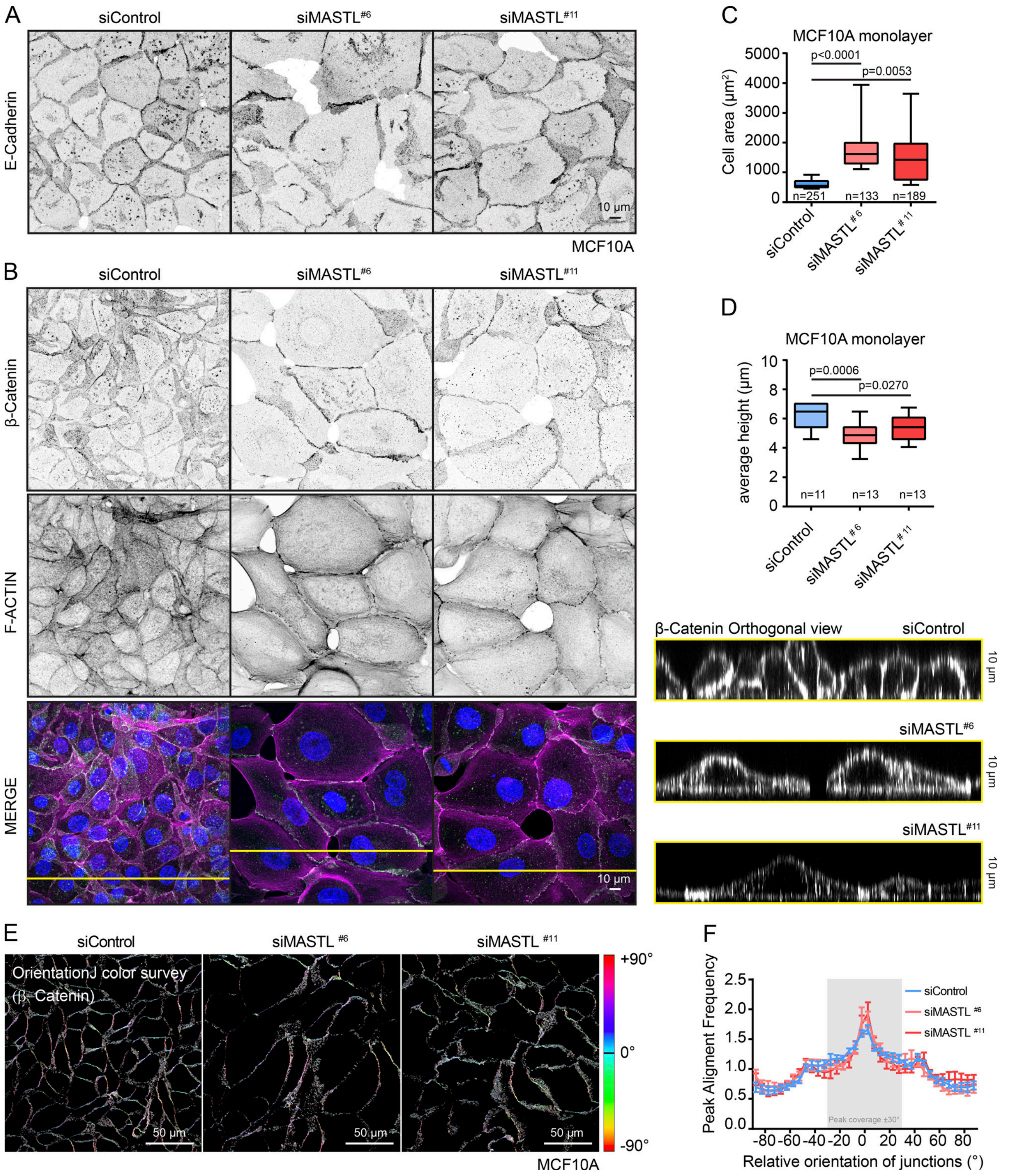

Figure 3. **MASTL regulates cell spreading, but not junctional orientation, of confluent MCF10A cells. (A and B)** Representative images of E-cadherin, β-catenin, F-actin (Phalloidin-Atto), and DAPI staining, and orthogonal view of the monolayer in siControl and siMASTL (48 h silencing) confluent MCF10A cultures. Images were acquired on a 3i CSU-W1 spinning disk confocal. **(C)** Quantification of cell area in a monolayer based on β-catenin staining (three independent experiments, with 251 [siControl], 133 [siMASTL#6], or 189 [siMASTL#11] cells in total). **(D)** Quantification of relative height of monolayer based on β-catenin staining (three independent experiments, 11 [siControl], 13 [siMASTL#6], or 13 [siMASTL#11] images in total). **(E)** Representative images of the local orientation of β-catenin–stained junctions represented by the corresponding color assigned to each specific angle of orientation, from −90° to 90°. **(F)** Analysis of cell–cell junction orientation in control and MASTL-silenced cells according to β-catenin staining using the OrientationJ ImageJ plugin (see Materials and methods). Frequency distributions of relative junctional orientations were then averaged over 12 images per condition, and the frequency of junction alignment was calculated across the ±30° spanning the peak. See also Table S1.

Downloaded from http://rupress.org/jcb/article-pdf/219/6/e201906204/1615651/jcb_201906204.pdf by guest on 09 February 2026

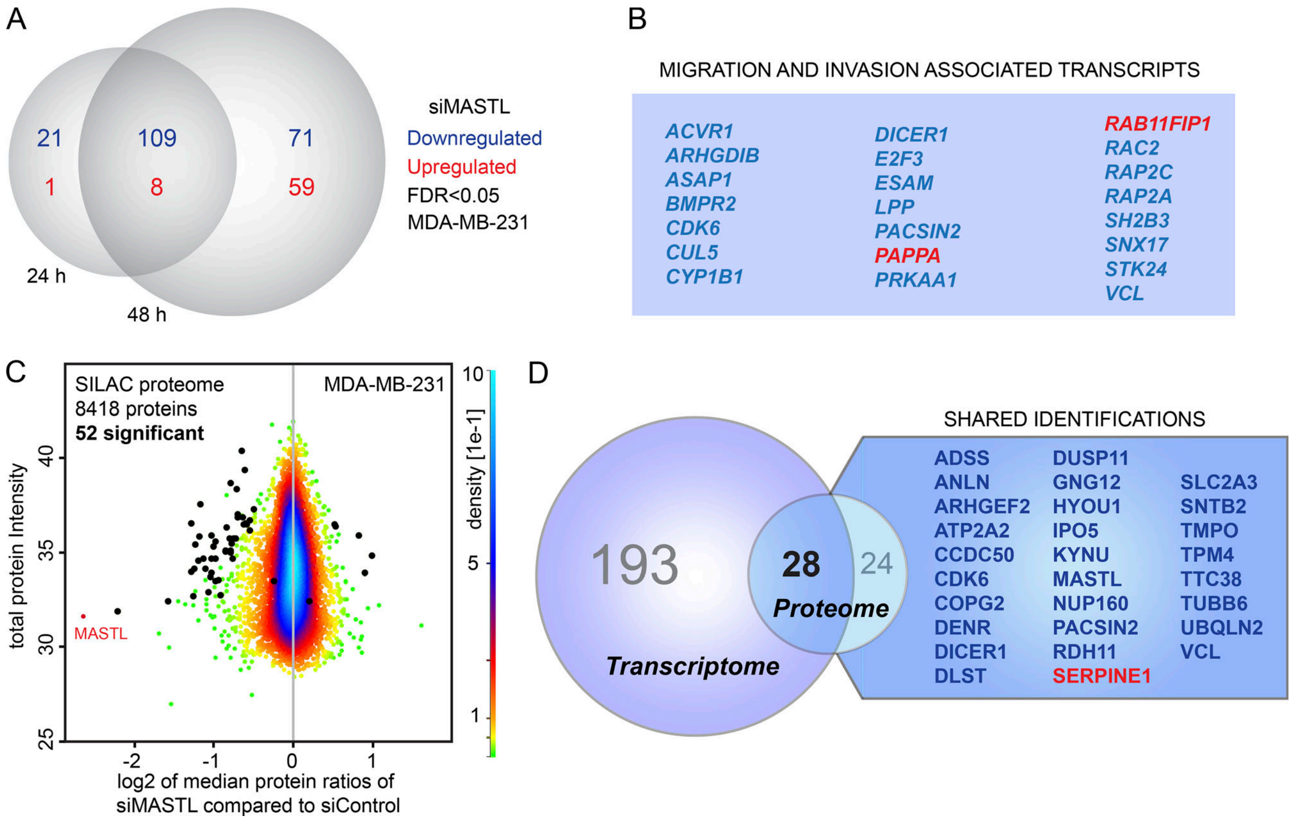

Figure 4. **MASTL supports expression of cell movement– and actin cytoskeleton–related genes. (A)** Venn diagram of differentially expressed transcripts (FDR < 0.05) measured with Illumina HT-12 at 24 h and 48 h after MASTL silencing in MDA-MB-231 cells. **(B)** Migration- and invasion-associated transcripts affected at RNA level after MASTL silencing according to Ingenuity Pathway Analysis. **(C)** A density scatterplot of SILAC proteome data displaying log2 of median protein ratios (siMASTL compared with siControl MDA-MB-231 cells) and total protein intensity. Each dot represents a protein. The color scale of the data point density is indicated on the right. Highlighted black circles represent significantly regulated proteins according to the significance B test. **(D)** List of differentially regulated hits identified in both the transcriptome and the total proteome datasets (shared identification). Blue, down-regulated hits; red, up-regulated hits. See also Fig. S3 and Table S2 and Table S3.

off-target effects of RNAi. Expression of EGFP-GEF-H1 in MASTL-depleted MDA-MB-231 cells significantly reduced spreading of MASTL-silenced cells (Fig. 5, J and K; and Fig. S4 E), indicating that GEF-H1–mediated contractility can overcome the effect of MASTL depletion on cell spreading.

High MASTL levels promote contractile actin stress fibers

Next, we studied how MASTL affects the actin cytoskeleton and phosphorylation of the myosin light chain (MLC), a key regulator of actomyosin contraction (Murrell et al., 2015). We plated MDA-MB-231 cells on collagen-coated crossbow-shaped micropatterns to normalize cell shape and facilitate comparisons between control and MASTL-silenced cells. In control cells, there were notable phosphorylated MLC (pMLC)–positive actin stress fibers across the cell. In contrast, a large proportion of MASTL-depleted cells displayed a reduced number of actin stress fibers and the accumulation of actin at the cell edge, resulting in broader lamellipodial actin structures (Fig. 6, A–C). In addition, and in line with immunofluorescence images, total pMLC levels were lower in MASTL-depleted cells (Fig. 6, D and E), and levels were restored by reexpression of siRNA-resistant EGFP-MASTL (Fig. 6 F). These results imply that silencing of MASTL decreases stress fiber formation and actomyosin contraction.

MASTL supports cell migration

Actin dynamics and actomyosin contraction play central roles in cell migration (Pollard and Cooper, 2009; Rottner et al., 2017). As MASTL depletion affected key regulators of actomyosin contraction and contractile actin fibers, we studied the migration properties of the cells using live-cell imaging (Fig. 7 A and Videos 1 and 2). Control-silenced cells moved rapidly with a prominent leading edge. In contrast, MASTL-silenced cells were round, flat, and stationary with significantly reduced cell migration distance (Fig. 7, B and C; and Fig. S4 F validation with a second siRNA oligo). Similar flat morphology has been detected in MASTL-silenced thyroid cancer cells recently (Cetti et al., 2019). This was not due to MASTL regulation of focal adhesion dynamics. Live-cell imaging of mEmerald-paxillin–labeled control and MASTL-silenced cells showed no significant differences in focal adhesion assembly or disassembly kinetics (Fig. 7 D–G; and Video 3). Accordingly, MASTL silencing had no effect on paxillin phosphorylation, an established regulator of focal adhesion turnover (Zaidel-Bar et al., 2007; Fig. 7, H and I). Importantly, increasing cell contractility through overexpression of GEF-H1 was not sufficient to rescue migration of MASTL-silenced cells (Fig. S4 F). These results suggest that MASTL depletion, leading to reduced levels of key cellular movement regulators, triggers defective cell migration.

Downloaded from http://rupress.org/jcb/article-pdf/219/6/e201906204/1615651/jcb_201906204.pdf by guest on 09 February 2026

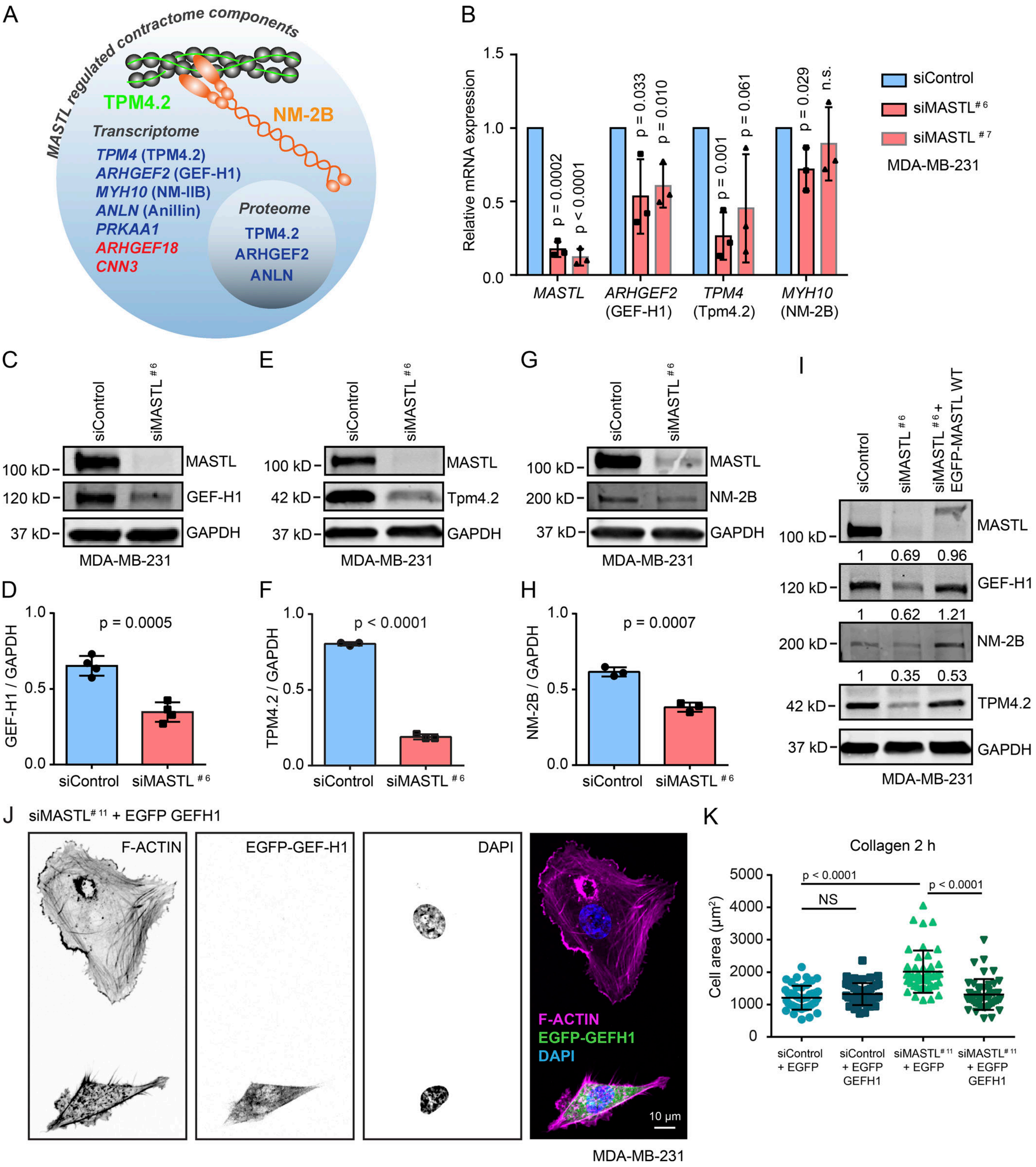

Figure 5. **MASTL induces GEF-H1, Tpm4.2, and NM-2B levels. (A)** Comparison of the transcriptome and proteome of MASTL-silenced MDA-MB-231 cells with known contractome-associated factors (Zaidel-Bar et al., 2015). **(B)** Quantification of relative mRNA levels of *MASTL*, *ARHGEF2*, *TPM4* and *MYH10* after MASTL silencing (48 h) in MDA-MB-231 cells based on real-time PCR analysis. **(C-H)** Western blot analysis and quantifications of GEF-H1, Tpm4.2, NM-2B, and MASTL protein levels in siControl and siMASTL MDA-MB-231 cells. Protein levels are normalized to GAPDH. **(I)** Western blot analysis of NM-2B, GEF-H1, and Tpm4.2 protein levels in siControl, siMASTL, or siMASTL + EGFP-MASTL (24 h MASTL silencing + 24 h expression of siRNA-resistant EGFP-MASTL) MDA-MB-231 cells. Mean protein levels quantified from three independent experiments relative to GAPDH are shown above indicated blots. **(J)** Representative F-actin (Phalloidin-Atto) and DAPI staining in siMASTL MDA-MB-231 cells transfected with EGFP-GEF-H1 for 24 h and plated on collagen for 2 h. Images were acquired on a 3i CSU-W1 spinning disk confocal. **(K)** Quantification of cell area based on the F-actin staining of 45 cells/condition in total (three independent experiments) from J. Data in all graphs are from three (B, F, and H) or four (D) biologically independent experiments (unpaired *t* test, mean ± SD). See also Table S1 and Fig. S4.

Downloaded from http://rupress.org/jcb/article-pdf/219/6/e201906204/1615651/jcb_201906204.pdf by guest on 09 February 2026

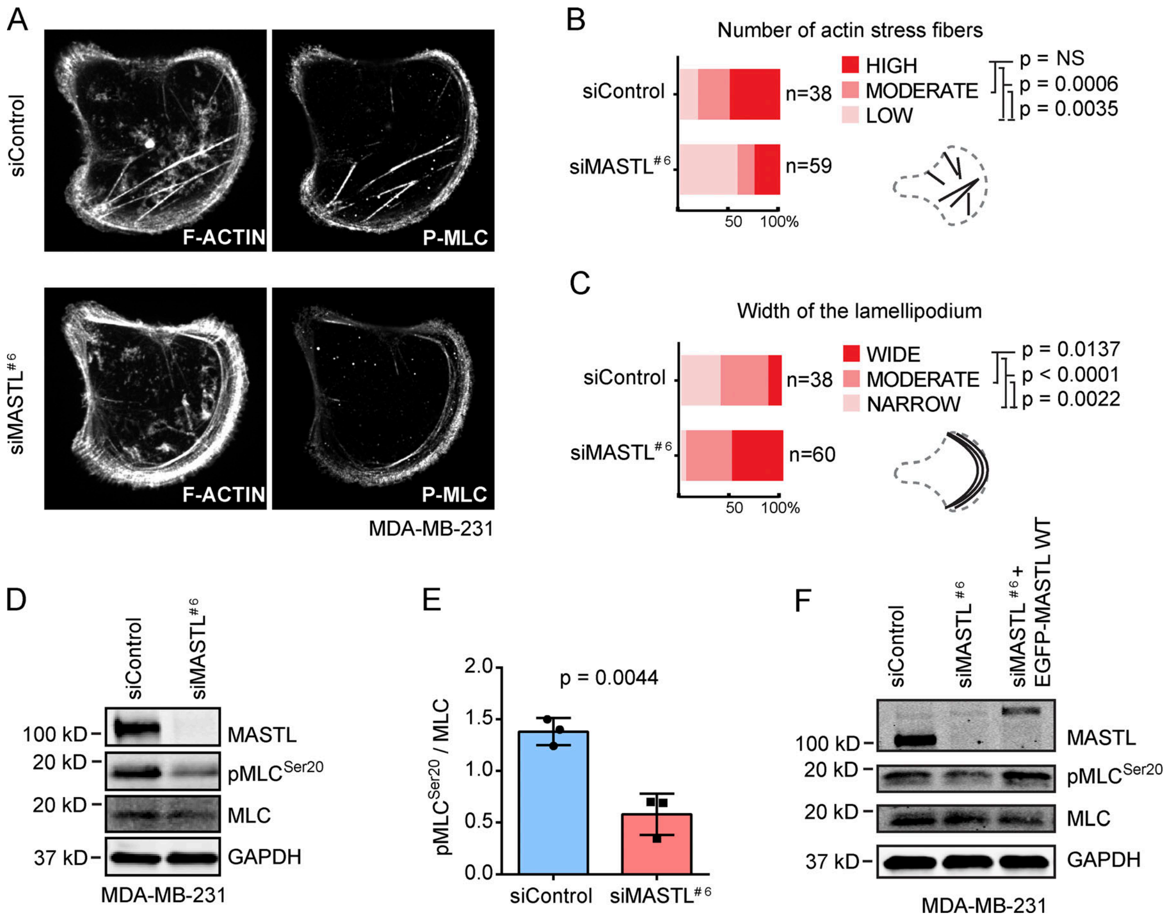

Figure 6. **High MASTL levels promote contractile actin stress fibers. (A)** Representative images of F-actin (Phalloidin-Atto) and pMLC (Thr18/Ser19) staining in siControl and siMASTL MDA-MB-231 cells plated on collagen-coated crossbow-shaped micropatterns (37 µm). **(B)** Quantification of the number of actin stress fibers in A (low, no obvious stress fibers; moderate, one to four stress fibers; high, five or more stress fibers). **(C)** Analysis of lamellipodium width from A, 38 (siControl) or 59 (siMASTL) cells in total. The width of the lamellipodium was measured from the widest point of the lamellipodium, 38 (siControl) or 60 (siMASTL) cells in total (narrow, 0–1.2 µm; moderate, 1.2–2 µm; and wide, >2 µm; *n* = 3 biologically independent experiments, Fisher's exact test). **(D)** Western blot analysis of phosphorylated (Ser20) and total MLC (pMLC and MLC, respectively) and MASTL protein levels in siControl and siMASTL MDA-MB-231 cells. GAPDH was used as a loading control. **(E)** Quantification of pMLC relative to total MLC protein levels after MASTL silencing (*n* = 3 biologically independent experiments, unpaired *t* test, mean ± SD). **(F)** Western blot analysis of pMLC (Ser20) and total MLC, MASTL and GAPDH protein levels in siControl, siMASTL, and siMASTL + EGFP-MASTL (24 h MASTL silencing + 24 h expression of siRNA-resistant EGFP-MASTL) MDA-MB-231 cells. Shown is a representative blot of three biologically independent experiments with similar results. See also Table S1.

MASTL regulates SRF activity kinase activity independently

SRF and MRTF-A are key regulators of cell motility as they jointly regulate transcription of genes related to actin dynamics, cell adhesion, and actomyosin contraction (Gau and Roy, 2018; Olson and Nordheim, 2010). As Tpm4.2 is a known target of SRF (Esnault et al., 2014) and GEF-H1 has been shown to induce SRF (Itoh et al., 2014), we decided to investigate the influence of MASTL on SRF activity. In MCF10A cells, MASTL depletion down-regulated mRNA levels of the established SRF target genes *VCL* (vinculin) and *FOS* (Fig. 8 A). Total protein levels of vinculin were also significantly decreased, while levels of paxillin, which is not an SRF target gene, remained unchanged following MASTL depletion (Fig. 8, B and C; and Fig. S5 A). Accordingly, there was less vinculin in focal adhesions of MASTL-silenced MCF10A cells (Fig. S5 B). Even though vinculin levels were lower in MASTL-silenced (two independent siRNA oligos) MCF10A cells, vinculin was still observed at cell–cell junctions (Fig. S5 C). Importantly, MASTL silencing, in MCF10A cells stably expressing the MRTF-SRF luciferase reporter, blocked serum-induced SRF transcriptional activity to a similar extent than SRF silencing with a validated specific siRNA (Hinojosa et al., 2017; Fig. 8 D). Conversely, overexpression of WT and kinase-dead MASTL augmented serum-induced SRF transcriptional activity (Fig. 8 E). These results indicate that MASTL expression, but not kinase function, is required for SRF activity and expression of SRF target genes.

Recently, a mutation (E167D) in MASTL has been linked to thrombocytopenia and cytoskeletal defects in platelets, indicative of a loss-of-function mutation (Hurtado et al., 2018). We generated the corresponding mutant (EGFP-MASTL-E167D) and found that it had no significant effect on SRF activity when overexpressed in cells expressing endogenous MASTL (Fig. S5 D), implying that E167D mutant MASTL is unable to induce SRF activity.

Downloaded from http://rupress.org/jcb/article-pdf/219/6/e201906204/1615651/jcb_201906204.pdf by guest on 09 February 2026

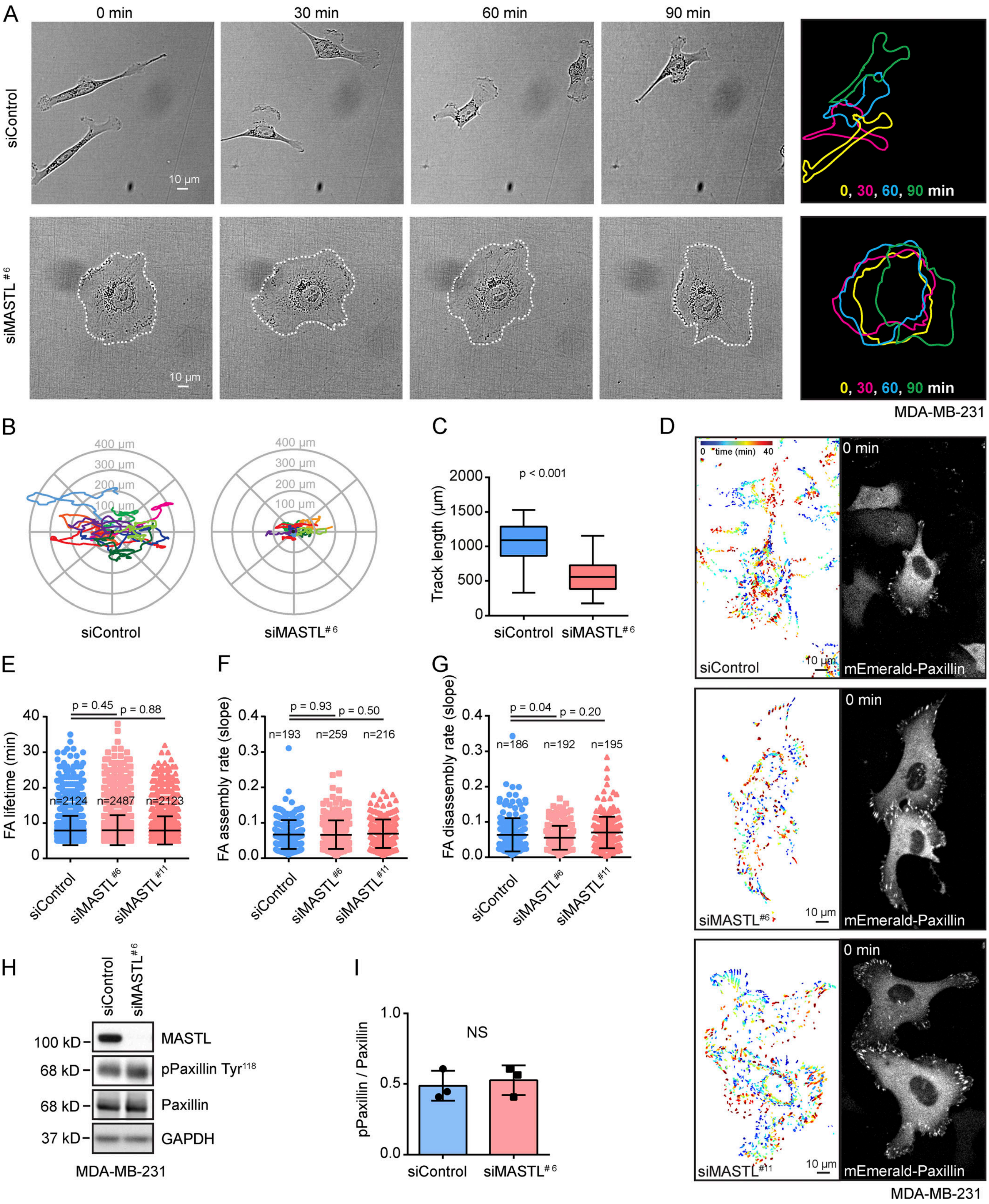

Figure 7. **MASTL supports cell migration without influencing focal adhesion dynamics. (A)** Representative phase contrast images from a 90-min time-lapse movie of siControl and siMASTL MDA-MB-231 cells (Nikon Eclipse Ti-E widefield microscope, Hamamatsu Orca C13440 Flash 4.0 ERG [b/w] sCMOS camera and Plan Apo lambda 20×/0.80, WD 1,000-µm objective). **(B)** Migration maps based on X and Y coordinates of siControl and siMASTL cells, recorded every 10 min, 700 min in total (9 tracks per condition shown with different colors; Nikon Eclipse Ti-E widefield microscope). **(C)** Migration track length of siControl and siMASTL cells (45 cells/condition in total, n = 3 biologically independent experiments, mean ± SD, unpaired t test with Welch's correction).

Downloaded from http://rupress.org/jcb/article-pdf/219/6/e201906204/1615651/jcb_201906204.pdf by guest on 09 February 2026

(D–G) Quantitative image analysis of focal adhesion dynamics based on live-cell imaging of endogenously tagged mEmerald-Paxillin in MDA-MB-231 cells. Visualization of the entire set of focal adhesions recorded every minute for a total of 40 min (D). Quantification of focal adhesion lifetime (E), focal adhesion assembly rate (F), and focal adhesion disassembly rate (G). Total number of cells/condition is indicated in the figure and Table S1. **(H)** Western blot analysis of MASTL, phospho-paxillin (Tyr118), and paxillin levels in siControl and siMASTL (48 h silencing) MDA-MB-231 cells. GAPDH used as a loading control. **(I)** Quantification of phospho-paxillin relative to paxillin after MASTL silencing (n = 3 biologically independent experiments, unpaired t test, mean ± SD). See also Table S1.

MRTF-A binds G-actin, and signal-regulated changes in cellular G-actin concentration control the nuclear translocation of this complex. However, depletion of MASTL had no effect on F-actin/G-actin ratio in MCF10A cells under normal growth conditions, whereas the actin filament polymerizing and stabilizing drug jasplakinolide significantly increased the ratio, serving as a positive control for the assay (Fig. S5, E and F).

MASTL associates with MRTF-A and regulates nuclear retention of MRTF-A

SRF and MRTF-A coregulate cytoskeletal genes following nuclear translocation of MRTF-A from the cytoplasm to the nucleus (Miralles et al., 2003). In line with the significantly reduced SRF activity in MASTL-depleted cells, we observed that MASTL depletion clearly attenuates serum-induced nuclear translocation of MRTF-A compared with control cells (Fig. 9 A). Conversely, overexpression of WT and kinase-dead MASTL augmented nuclear MRTF-A localization in response to serum (Fig. 9 B). Interestingly, the MASTL E167D patient mutant was unable to accelerate nuclear location of MRTF-A (Fig. 9 B), in line with its inability to augment SRF activity. These data suggest that MASTL is required for efficient signal-regulated nuclear translocation of MRTF-A and SRF activation independently of an effect on the F-actin/G-actin ratio.

In line with earlier publications, we find that MASTL is predominantly nuclear (Fig. 1, D and G). This prompted us to investigate whether MASTL associates with MRTF-A. Endogenous MRTF-A was readily detected from GFP pull-downs of EGFP-MASTL WT and EGFP-MASTLG44S, but not GFP alone, in MCF7 cells (Fig. 9 C). Finally, fluorescence loss in photobleaching (FLIP) analysis of MRTF-A nuclear retention through repeated bleaching of the cytoplasmic MRTF-A pool revealed that MASTL

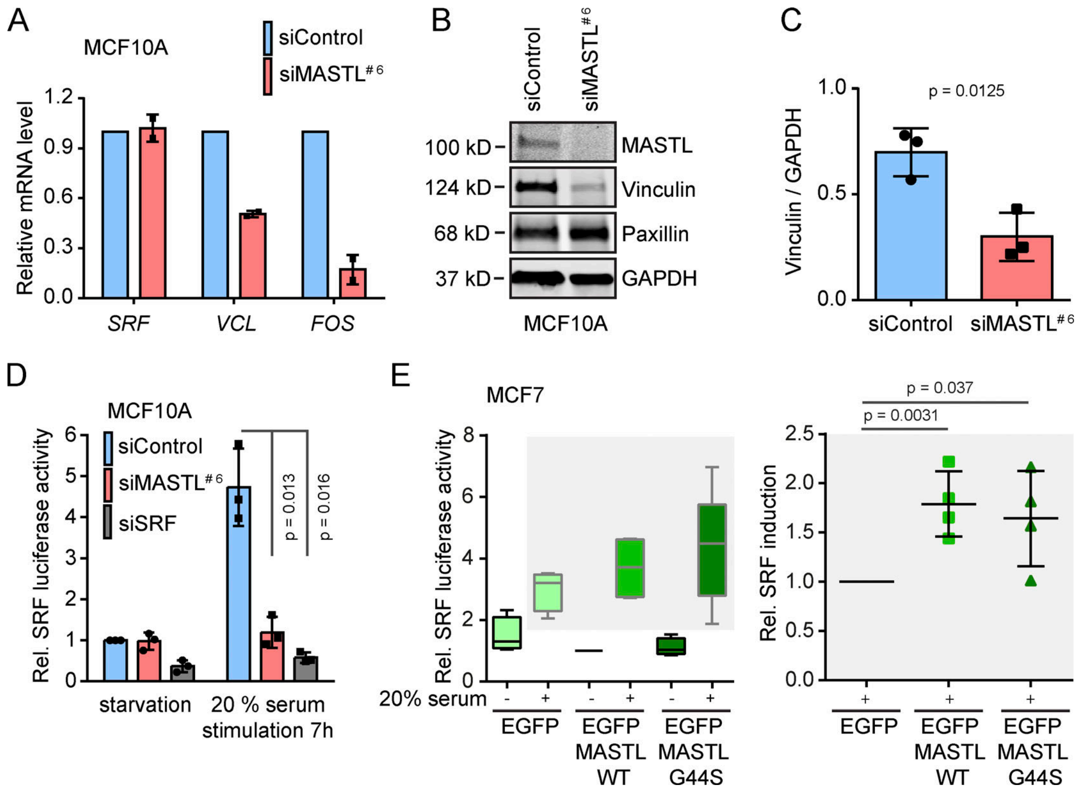

Figure 8. **MASTL regulates SRF activity independent of its kinase activity. (A)** Quantification of *SRF*, *VCL*, and *FOS* mRNA levels relative to TATA-box binding protein (TBP) in siMASTL (72 h silencing) MCF10A cells (n = 2 biologically independent experiments, mean ± SD). **(B)** Western blot analysis of vinculin, paxillin, and MASTL protein levels in siControl and siMASTL MCF10A cells after 48 h of silencing. GAPDH was used as a loading control. **(C)** Quantification of vinculin levels in B after MASTL silencing. Protein levels are normalized to GAPDH (n = 3 individual experiments). **(D)** Relative SRF luciferase activity in siControl, siMASTL and siSRF (SRF-silenced) MCF10A cells following 48 h of silencing under serum-starved conditions and after stimulation with 20% serum (n = 3 individual experiments). **(E)** Relative SRF luciferase activity. MCF7 cells expressed EGFP control, EGFP-MASTL WT, and EGFP-MASTL G44S together with the SRF reporter 3D.Aluc and RLTK Renilla luciferase transfection control under serum-starved conditions and after stimulation with 20% serum (n = 4 individual experiments). Unpaired t test and mean ± SD is used in all graphs. See also Table S1.

Downloaded from http://rupress.org/jcb/article-pdf/219/6/e201906204/1615651/jcb_201906204.pdf by guest on 09 February 2026

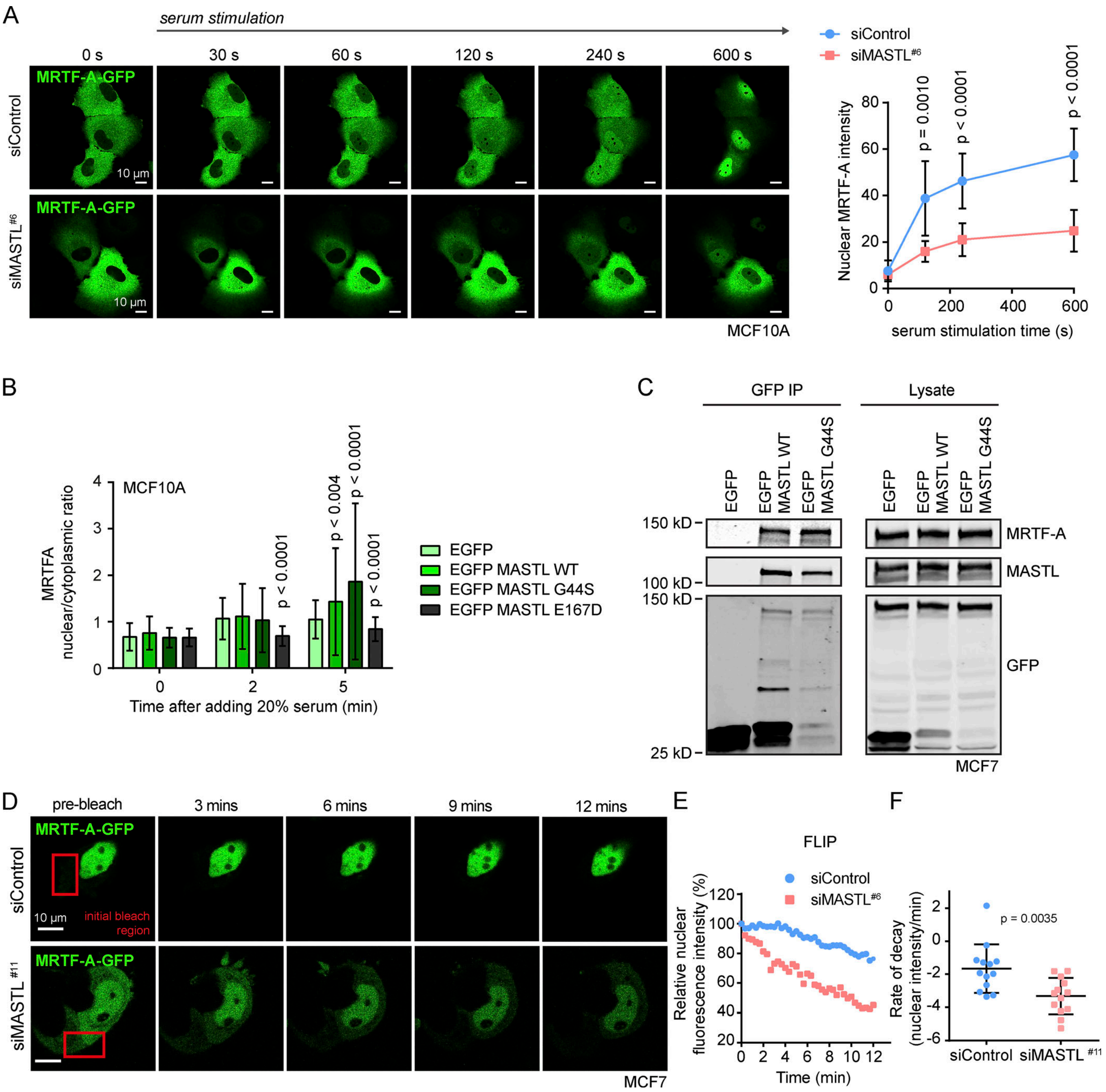

Figure 9. **MASTL associates with MRTF-A and regulates nuclear retention of MRTF-A. (A)** Live-cell imaging of siControl and siMASTL MCF10A cells stably expressing pIND20-MRTF-A-GFP. Cells were serum starved (24 h) before imaging and MRTF-A-GFP translocation was followed after adding 20% serum (LSM 800 confocal microscope; Zeiss). Analysis of MRTF-A nuclear intensity in siControl and siMASTL cells 0, 120, 240, and 600 s after serum stimulation based on live-cell imaging of 8–9 cells/condition is shown (*n* = 3 independent experiments). **(B)** Nuclear/cytoplasmic ratio of MRTF-A in EGFP control, EGFP-MASTL WT, EGFP-MASTL G44S, and EGFP MASTL E167D–overexpressing MCF7 cells fixed 0, 2, or 5 min after adding serum and stained for MRTF-A (*n* = 3 independent experiments). **(C)** Western blot of MRTF-A and MASTL in GFP immunoprecipitations and original lysate in EGFP control, EGFP-MASTL WT, and EGFP-MASTL G44S–overexpressing MCF7 cells (*n* = 3 independent experiments). **(D-F)** FLIP representative images (D) and analysis (E and F) of MRTF-A nuclear translocation through repeated bleaching of the cytoplasmic MRTF-A-GFP pool in siControl and siMASTL MCF7 cells after 10 min of serum stimulation. Representative fluorescence intensity curves from two individual cells (E) and quantification of rate of decay (F) are shown (*n* = 3 biological replicates, with 13 cells in total/condition). See also Table S1.

silencing significantly enhances loss of nuclear GFP-MRTF-A signal compared with control cells (Fig. 9, D–F). Taken together, these data indicate that MASTL associates with MRTF-A and supports nuclear retention of MRTF-A in cells.

Silencing of MASTL inhibits cancer cell invasion and regulates cell morphology in 3D

Our data demonstrate MASTL as a key regulator of MRTF-A localization and activity. Next we compared the effects of MRTF-A

Downloaded from http://rupress.org/jcb/article-pdf/219/6/e201906204/1615651/jcb_201906204.pdf by guest on 09 February 2026

and MASTL silencing. Silencing of MRTF-A induced cell spreading (Fig. 10, A and B) and decreased the expression of vinculin, an established SRF target gene (Miralles et al., 2003), but not paxillin (Fig. 10 C), similarly to MASTL silencing (Figs. 2 A and 8 B). GEF-H1 levels were not decreased by MRTF-A silencing, in line with the notion that GEF-H1 is not an SRF target gene (Itoh et al., 2014; Ly et al., 2013). These results indicate that MRTF-A activation downstream of MASTL is a key regulatory step in cell spreading. To investigate this further, we analyzed cell invasion in three-dimensional extracellular matrix. Depletion of MRTFs or SRF is known to reduce MDA-MB-231 cell invasion (Medjkane et al., 2009). We found that silencing of MASTL significantly inhibits MDA-MB-231 invasion into a fibronectin-supplemented collagen I gel, similar to MRTF-A silencing (Fig. 10, D and E). In addition, MASTL- or MRTF-A–silenced cells were rounder than the elongated control cells (Fig. 10, F and G). Importantly, MASTL silencing reduced nuclear localization of endogenous MRTF-A in cells in 3D (Fig. 10, H and I), suggesting that MASTL is required for MRTF-A–regulated cancer cell invasion in 3D.

Discussion

We describe here an original kinase-independent function for the well-recognized mitosis accelerator, MASTL, in regulating cell morphology. Our data establish an intimate link between the predominantly nuclear MASTL and regulation of cell adhesion, cell contractility, spreading, and motility. We demonstrate that MASTL localizes to the nucleus, associates with MRTF-A and is necessary for the full activity of the MRTF/SRF signaling pathway, a key coordinator of gene transcription and cytoskeletal dynamics (Esnault et al., 2014). MASTL regulates a transcriptional contractility/adhesion program in normal epithelial cells and carcinoma cells, suggesting that our data establish a fundamentally important original pathway to control cell architecture (Fig. 10 J).

We find that depletion of MASTL renders cells nearly stationary with a very flat morphology devoid of obvious front-rear polarity. MASTL overexpression also reduces directionality of cell migration in MCF10A cells (Rogers et al., 2018), suggesting that the levels of MASTL must be tightly regulated to maintain optimal cell morphology for migration. The exact mechanism of MASTL-induced cell motility and the role of its kinase activity in regulating cell morphology has not been investigated in detail. Contractility affects the dynamic properties of the actin cytoskeleton and its organization into lamellipodia and stress fibers (Hirata et al., 2008; Hotulainen and Lappalainen, 2006; Medeiros et al., 2006; Wilson et al., 2010). Therefore, our data linking MASTL to contractility, through kinase-independent activation of the MRTF–SRF pathway and positive regulation of GEF-H1, is likely to be a central mechanism in MASTL regulation of cell morphology. Previous work has indicated that kinase activity is necessary for MASTL overexpression–induced migration of MDA-MB-231 cells (Vera et al., 2015), whereas we find that MASTL regulation of cell spreading and MRTF-A-SRF signaling are independent of kinase function. Currently, the reason for these somewhat discrepant findings is unclear. Recently, thrombocytopenia-associated mutations in MASTL (including E167D) were shown to cause actin cytoskeletal alterations in postmitotic platelets, suggesting that these are loss-of-function mutations and indicating a clinically relevant role for MASTL linked to the regulation of the cytoskeleton (Hurtado et al., 2018). Accordingly, we find that the patient mutation E167D renders MASTL inactive in augmenting SRF activity. In breast cancer xenograft models, high MASTL levels have been shown to positively correlate with tumor growth, invasion, and metastasis (Álvarez-Fernández et al., 2018; Rogers et al., 2018; Vera et al., 2015). We show here that silencing MASTL impairs cell invasion in 3D, further supporting the notion of MASTL as an important regulator of cell motility in different biological contexts.

We found that MASTL was required for efficient serum-induced nuclear translocation of MRTF-A and that this is independent of MASTL kinase activity. MRTFs are predominantly cytoplasmic in unstimulated cells, yet they continuously shuttle through the nucleus. Signal-induced G-actin depletion (through increased actin polymerization) decreases MRTF–actin interaction in both the nucleus and cytoplasm and promotes MRTF nuclear accumulation (Baarlink et al., 2013; Guettler et al., 2008; Miralles et al., 2003; Vartiainen et al., 2007). We found no significant difference in the F-actin/G-actin ratio of MASTL-depleted cells. However, we found that MASTL associates with MRTF-A and increases nuclear retention of MRTF-A. Thus, the cell motility and contractility-promoting activities of MASTL seem to be mediated through MRTF-A (and possibly through other currently unknown mechanisms), but not through regulation of G-actin levels.

We find that MASTL intersects with the Rho pathway through regulating the expression of GEF-H1. Down-regulation of GEF-H1 upon MASTL silencing correlates with increased cell spreading and reduced stress-fiber formation, indicating a role for GEF-H1 in the phenotype. However, unlike the other MASTL-regulated genes/proteins studied here, GEF-H1 has not been described as an SRF-target gene. Instead, GEF-H1 is a known inducer of SRF (Itoh et al., 2014; Ly et al., 2013). This implies that MASTL may regulate cell spreading also through SRF-transcription–independent mechanisms that further enhance MASTL-mediated positive regulation of this signaling pathway. GEF-H1 is a multifunctional protein implicated in processes such as vesicle traffic (Pathak et al., 2012), cytokinesis (Birkenfeld et al., 2008), endomitosis (Gao et al., 2012), G1/S phase transition (Aijaz et al., 2005), cytokine production (Wang et al., 2017), sensing of foreign RNA (Chiang et al., 2014), and cellular adaptation to force (Guilluy et al., 2011). Importantly, GEF-H1 is shown to be an oncogenic driver (Cullis et al., 2014). Therefore, the link between MASTL and GEF-H1, revealed here, most likely has a strong impact on a wide range of biological processes.

MASTL overexpression in MCF10A cells increases aberrant mitotic divisions resulting in increased micronuclei formation (Rogers et al., 2018). Contractility is a key player in cell division. It affects the assembly of the mitotic spindle architecture, function, and orientation (Carreno et al., 2008; Chaigne et al., 2013; Kunda et al., 2008; Théry et al., 2005). In the following step, cytokinesis, the separation of the two cells relies on the

Downloaded from http://rupress.org/jcb/article-pdf/219/6/e201906204/1615651/jcb_201906204.pdf by guest on 09 February 2026

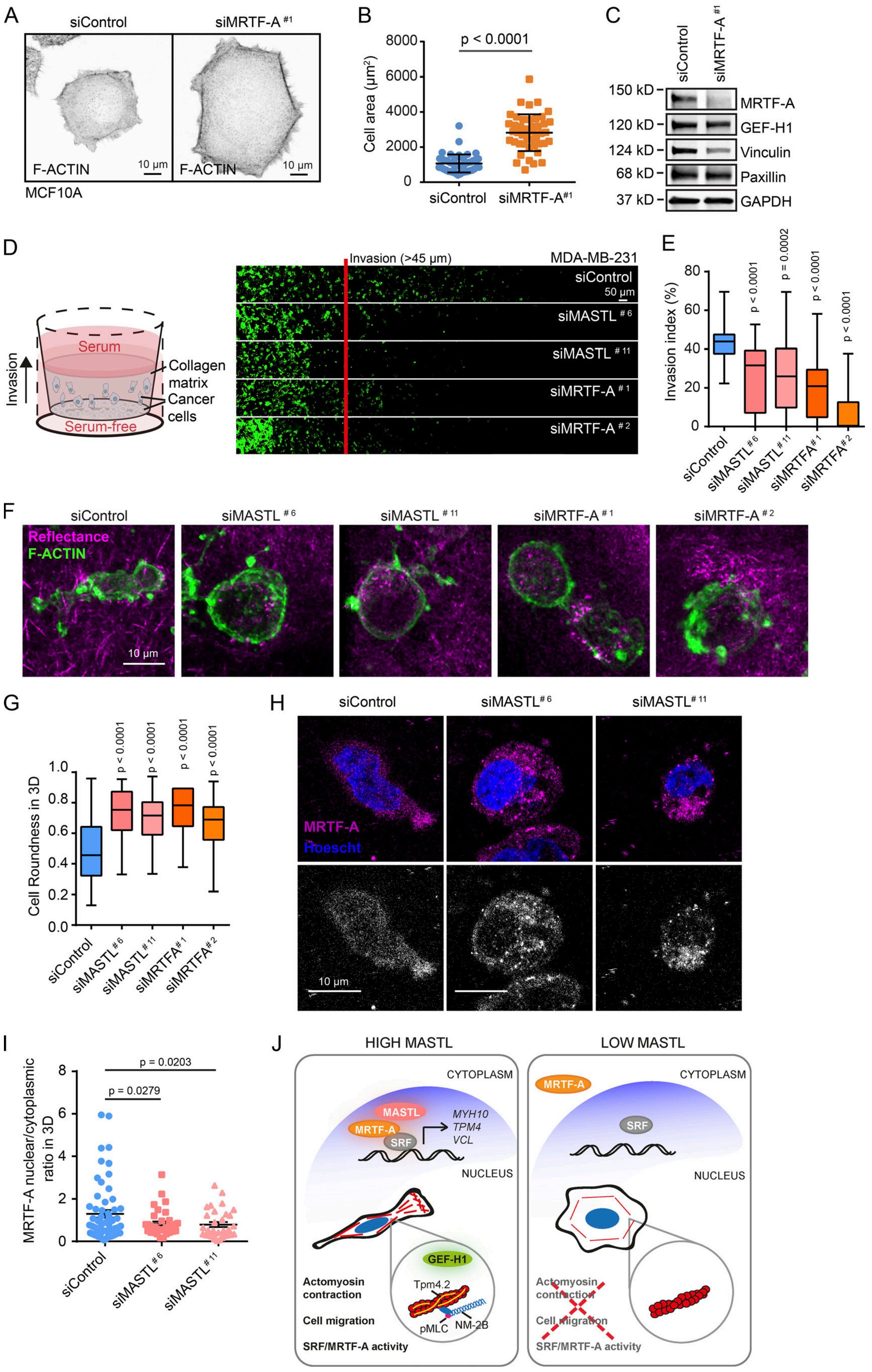

Downloaded from http://rupress.org/jcb/article-pdf/219/6/e201906204/1615651/jcb_201906204.pdf by guest on 09 February 2026

Figure 10. **Silencing of MASTL inhibits cancer cell invasion and regulates cell morphology in 3D. (A)** Representative images of F-actin (Phalloidin-Atto) staining in siControl and siMRTF-A–silenced (48 h) MCF10A cells plated on collagen for 2 h. Images were acquired on a 3i CSU-W1 spinning disk confocal. **(B)** Quantification of cell area based on the F-actin staining of 45 cells (three independent experiments, unpaired *t* test). **(C)** Western blot analysis of MRTF-A, GEF-H1, vinculin, paxillin, and GAPDH protein levels in siControl and siMRTF-A–silenced (48 h) MCF10A cells. **(D–G)** Inverted invasion assessment of siControl, siMASTL, and siMRTF-A MDA-MB-231 cells. Schematic illustration of the invasion assay used and representative images for each condition after 96 h invasion and staining with phalloidin-488; *n* = 3 biological replicates, with nine stacks/condition/replicate, mean ± SD, unpaired *t* test with Welch's correction (D), along with quantification (E). Representative high-magnification images (F) and quantification (G) of invading MDA-MB-231 cells assessed for their roundness (*n* = 3 biological replicates, with at least seven cells/condition/replicate, mean ± SD, unpaired *t* test with Welch's correction;). **(H and I)** Representative high-magnification images of MRTF-A staining and Hoechst (H) and MRTF-A nuclear/cytoplasmic ratio quantification (I) of invading MDA-MB-231 cells. **(J)** Schematic illustrating how MASTL regulates cell morphology, migration, and transcription of actin regulators by controlling the nuclear localization of MRTF-A and SRF activity. Data in all graphs are from *n* = 3 biologically independent experiments (mean ± SD). See also Table S1.

actomyosin-derived forces generating the cleavage furrow contractile zone (Mendes Pinto et al., 2013; Pollard, 2010). Thus far, the majority of studies have focused on MASTL regulating mitosis through the MASTL–ENSA–PP2A–B55 axis through phosphorylation of ENSA (Vigneron et al., 2016). However, our data showing kinase-activity independent MASTL regulation of cell contractility and expression of cell adhesion/architecture regulating proteins suggests that MASTL may contribute to faithful cell division also through additional mechanisms.

Mechanistically, MASTL has been suggested to support oncogenicity by repression of the tumor suppressor activity of PP2A-B55, increase in chromosome instability or deregulation of the phosphoinositide 3-kinase-AKT-mammalian target of rapamycin (PI3K–AKT–mTOR) pathway (Marzec and Burgess, 2018). Our data suggest an additional mechanism where MASTL regulates actin morphology, adhesion, and migration of cells via transcriptional control, which could have a highly important role in cancer metastasis. In fact, drugs that would target contractility (migrastatics) are suggested to work as anticancer therapy for invasion and metastasis, the leading cause of mortality in solid cancers (Gandalovičová et al., 2017). Importantly, our transcriptome and proteome data provide a resource unveiling several cancer-associated factors that are down-regulated after MASTL depletion. This information may lead to further breakthroughs into the exact role of MASTL in cancer.

Materials and methods

Cell lines

MCF10A (human epithelial) cells were cultured in DMEM/Nutrient Mixture F-12 (Gibco) supplemented with 5% horse serum (Gibco), 20 ng/ml EGF (Sigma-Aldrich), 0.5 µg/ml hydrocortisone (Sigma-Aldrich), 100 ng/ml cholera toxin (Sigma), 10 µg/ml insulin (Sigma-Aldrich), and 1% penicillin-streptomycin (Sigma-Aldrich) in + 37°C, 5% CO_2.

MDA-MB-231 (human triple-negative adenocarcinoma; ATCC) cells were cultured in DMEM (Sigma-Aldrich) supplemented with 10% FBS (Sigma-Aldrich), 2 mM l-glutamine (Sigma-Aldrich), and 1% MEM nonessential amino acid solution (Sigma-Aldrich) in 37°C 5% CO_2.

MCF7 (human adenocarcinoma; ATCC) cells were cultured in DMEM supplemented with 10% FBS (Sigma-Aldrich) and 2 mM l-glutamine (Sigma-Aldrich) in 37°C 5% CO_2.

All of the cell lines were mycoplasma negative.

Antibodies, siRNAs, primers, and DNA constructs

Table 1 lists the antibodies, siRNAs, primers, and DNA constructs used in this study.

Transfections

Transfections of siRNAs were performed by using Lipofectamine RNAiMAX transfection reagent (Invitrogen) according to manufacturer's protocol.

Transfections of plasmid DNAs were performed by using Lipofectamine 2000 Transfection Reagent (Invitrogen).

Adhesion assays

Adhesion assays were performed by using xCELLigence cell analyzer RTCA (Roche). A 96-well E-Plate (Roche) was coated with 5 µg/ml of collagen (PureCol; INAMED BioMaterials), fibronectin (341631; Merck), or BSA (as a control) overnight at 4°C. Prior to the experiment, wells were blocked with 0.1% BSA in PBS for 3 h at 37°C and washed with PBS. 50 µl of MDA-MB-231 growth medium was added on each well, and background signals were measured using the xCELLigence analyzer. Silenced and/or transfected cells were detached by trypsinization, followed by trypsin inactivation with 10% FBS. Cells were centrifuged at 200 *g* to remove the serum, washed with serum-free growth medium, recentrifuged, and resuspended in serum-free medium. 2,000 cells diluted in 100 µl serum-free media were added on each well, and cell index values indicating the impedance between E-bottom electrodes were recorded immediately in real time using the xCELLigence analyzer.

Cell spreading and immunostaining

siRNA-treated and/or transfected MDA-MB-231, MCF10A, or MCF7 cells were plated on glass-bottom plates (MatTek) or µ-slide eight-well chambered coverslips (ibidi), which had been coated with 5 µg/ml collagen overnight at 4°C. Cells were allowed to adhere in full growth media for 2 h in 37°C 5% CO_2, fixed with 4% PFA, washed with PBS, and permeabilized with 0.1% Triton-X in PBS. MDA-MB-231 and MCF7 cells were stained with Phalloidin Atto-647N (1:200, 65906; Sigma-Aldrich) and 4′6-diamidino-2-phenylindole (DAPI, 1:10,000) in 1% BSA in PBS for 45 min at RT and washed with PBS. MCF10A cells were first stained with indicated primary antibodies in 1% BSA in PBS for 1 h at RT, washed with PBS, and incubated in Alexa Fluor secondary antibody (1:400), Phalloidin Atto-647N (1:200), and DAPI (1:10,000) in 1% BSA in PBS for 45 min at RT. For Tpm4.2 staining, cells were fixed with 1% PFA with 20 mM Hepes for

Downloaded from http://rupress.org/jcb/article-pdf/219/6/e201906204/1615651/jcb_201906204.pdf by guest on 09 February 2026

Table 1. **Antibodies, siRNAs, primers, and DNA constructs used in this study**

Reagent or resource	Source	Identifier
Antibodies		
Rabbit anti-MASTL (1:1,000 for Western blot [WB])	Sigma-Aldrich	Cat# HPA027175; RRID: AB_1853591
Rabbit anti-MASTL (1:1,000 for WB)	Abcam	Cat# ab86387; RRID:AB_1925198
Mouse anti-α-tubulin (1:1,000 for WB, 1:100 for immunofluorescence [IF])	Hybridoma bank	12g10anti-alpha-tubulin
Mouse anti-β1-integrin CD29 (1:1,000 for WB)	BD Biosciences	Cat# 610468; RRID:AB_397840
Mouse anti-GAPDH (1:20,000 for WB)	HyTest	Cat# 5G4MAB6C5
Mouse anti-paxillin (1:100 for IF, 1:1,000 for WB)	BD Biosciences	Cat# 612405, RRID:AB_647289
Rabbit anti-phospho-MLC 2 (Thr18/Ser19; 1:100 for IF)	Cell Signaling Technology	Cat# 3674, RRID:AB_2147464
Rabbit anti-MLC (phospho S20; 1:500 for WB)	Abcam	Cat# ab2480, RRID:AB_303094
Rabbit anti-MLC 2 (1:500 for WB)	Cell Signaling Technology	Cat# 3672, RRID:AB_10692513
Rabbit anti-GEF-H1 (1:1,000 for WB)	Cell Signaling Technology	Cat# 4076, RRID:AB_2060032
Rabbit anti-phospho-GEF-H1 (Ser886; 1:1,000 for WB)	Cell Signaling Technology	Cat# 14143, RRID:AB_2798402
Rabbit anti-tropomyosin 4.2 (Delta Tm 9d; 1:1,000 for WB, 1:100 for IF)	A kind gift from Prof. Peter Gunning (UNSW Sydney, Sydney, Australia)	(Schevzov et al., 2011)
Mouse anti-nonmuscle myosin IIB (1:1,000 for WB)	Abcam	Cat# ab684, RRID:AB_305661
Mouse anti-vinculin (1:100 for IF, 1:1,000 for WB)	Sigma-Aldrich	Cat# V9131, RRID:AB_477629
Mouse anti-β-actin (clone AC-15; 1:1,000 for WB)	Sigma-Aldrich	Cat# A1978, RRID:AB_476692
Recombinant anti-β-catenin antibody (E247; 1:100 for IF)	Abcam	Cat# ab32572, RRID:AB_725966
Rabbit anti-E-cadherin (24E10; 1:100 for IF)	Cell Signaling Technology	Cat# 3195, RRID:AB_2291471
Rabbit anti-GEF-H1 (IF 1:100)	Abcam	Cat# ab155785, RRID:AB_2818944
Rabbit anti-phospho-paxillin (Tyr118; 1:1,000 for WB)	Cell Signaling Technology	Cat# 2541, RRID:AB_2174466
Mouse anti-MRTF-A (G-8; 1:200 for IF)	Santa Cruz Biotechnology	Cat# sc-390324
Donkey anti-mouse IgG (H+L) highly cross-adsorbed secondary antibody, Alexa Fluor 568 (1:400 for IF)	Thermo Fisher Scientific	Cat# A10037, RRID:AB_2534013
Donkey anti-mouse IgG (H+L) highly cross-adsorbed secondary antibody, Alexa Fluor 488 (1:400 for IF)	Invitrogen	Cat# A-21202
IRDye 680RD donkey anti-mouse IgG (1:5,000 for WB)	LI-COR Biosciences	Cat# 926-68072
Donkey anti-rabbit IgG (H+L) highly cross-adsorbed secondary antibody, Alexa Fluor 488 (1:400 for IF)	Invitrogen	Cat# A-21206
IRDye 800CW donkey anti-rabbit IgG (1:5,000 for WB)	LI-COR Biosciences	Cat# 926-32213
siRNAs and primers		
AllStars negative control siRNA	Qiagen	1027281
Hs_MASTL_6 FlexiTube siRNA (target sequence 5′-ACGCCTTATTCTAGCAAATTA-3′)	Qiagen	SI02653014
Hs_MASTL_7 FlexiTube siRNA (target sequence 5′-CAGGACAAGTGTTATCGCTTA-3′)	Qiagen	SI02653182
Hs_MASTL_11 FlexiTube siRNA (target sequence 5′-CAGCCCTTAGATTCAGATAGA-3′)	Qiagen	SI04441066
Hs_MKL1_7 FlexiTube siRNA (target sequence 5′-ATCACGTGTGATTGACATGTA-3′)	Qiagen	SI04172028
MRTF-A (sense strand 5′-CCAUCAUUGUGGGCCAGGU-3′)	Sigma-Aldrich	PDSIRNA5D
Hs_SRF_5 FlexiTube siRNA (target sequence 5′-CAAGATGGAGTTCATCGACAA-3′)	Qiagen	SI02757622

Downloaded from http://rupress.org/jcb/article-pdf/219/6/e201906204/1615651/jcb_201906204.pdf by guest on 09 February 2026

Table 1. **Antibodies, siRNAs, primers, and DNA constructs used in this study (*Continued*)**

Reagent or resource	**Source**	**Identifier**
RT-PCR primer for ARHGEF2	Universal Probe Library (Roche)	
Forward: 5′-TACCTGCGGCGAATTAAGAT-3′		
Reverse: 5′-AAACAGCCCGACCTTCTCTC-3′		
Probe: 22		
RT-PCR primer for GAPDH	Universal Probe Library (Roche)	
Forward: 5′-GCCCAATACGACCAAATCC-3′		
Reverse: 5′-AGCCACATCGCTCAGACA-3′		
Probe: 60		
RT-PCR primer for MYH10	Universal Probe Library (Roche)	
Forward: 5′-GGAGGACACGCTGGACAC-3′		
Reverse: 5′-TCTGCCACTTCTTGTTCACG-3′		
Probe: 3		
RT-PCR primer for MASTL	Universal Probe Library (Roche)	
Forward: 5′-GTCTGCAAACAATGTCTACTTGGTA-3′		
Reverse: 5′-CTAGAGCCAGTGCTACTTCAGAAA-3′		
Probe: 76		
RT-PCR primer for TPM4	Universal Probe Library (Roche)	
Forward: 5′-CGGTGAAACGCAAGATCC-3′		
Reverse: 5′-GGCCACATCACCTTCAGC-3′		
Probe: 24		
qPCR primer for TBP	N/A	N/A
Forward: 5′-TGCACAGGAGCCAAGAGTGAA-3′		
Reverse: 5′-CACATCACAGCTCCCCACCA-3′		
qPCR primer for SRF	N/A	N/A
Forward: 5′-CAGATCGGTATGGTGGTCGG-3′		
Reverse: 5′-GTCAGCGTGGACAGCTCATA-3′		
qPCR primer for FOS	N/A	N/A
Forward: 5′-CTCTCTTACTACCACTCACCCGC-3′		
Reverse: 5′-GGTCCGTGCAGAAGTCCTGCG-3′		
qPCR primer for VCL	N/A	N/A
Forward: 5′-ACCAAGGCATAGAGGAAGCTTTA-3′		
Reverse: 5′-GCTCTCTTCATGGCTTCAGTG-3′		
DNA constructs		
pcDNA EGFP-C2	This paper	N/A
pcDNA EGFP MASTL WT (siRNA resistant)	This paper	N/A
pcDNA EGFP MASTL G44S (siRNA resistant)	This paper	N/A
pcDNA EGFP MASTL E167D (siRNA resistant)	This paper	N/A
pIND20-MRTF-A-GFP	Hinojosa et al., 2017	N/A
mEmerald-paxillin-22	A kind gift from Prof. Robert Grosse, Institute of Experimental and Clinical Pharmacology and Toxicology, University of Freiburg and CIBSS – Center for Integrative Biological Signalling Studies, Freiburg, Germany (plasmid 54219; Addgene; http://n2t.net/addgene:54219; RRID:Addgene_54219)	(Paszek et al., 2012)
pcDNA3.1 EGFP ARHGEF2	A kind gift from Prof. Michael Sixt (The Institute of Science and Technology Austria, Klosterneuburg, Austria)	Kopf et al., 2019 *Preprint*

Downloaded from http://rupress.org/jcb/article-pdf/219/6/e201906204/1615651/jcb_201906204.pdf by guest on 09 February 2026

30 min at 37°C, permeabilized with ice-cold methanol for 5 min at −20°C (which was slowly diluted out with PBS), and blocked with 5% BSA in PBS for 1 h.

Stained cells were washed with PBS and imaged with confocal microscope 3i Spinning Disk, Hamamatsu ORCA-Flash4.0 v2 scientific complementary metal-oxide semiconductor (sCMOS) camera (Hamamatsu Photonics), and Plan-Apochromat 63×, 1.4 NA oil objective, or with The Carl Zeiss LSM 880 Airyscan and C Plan-Apochromat 63×/1.4 Oil differential interference contrast UV-VIS-IR M27 (working distance [WD] 0.140 mm) objective. Cell and focal adhesion areas were analyzed by using ImageJ.

Focal adhesion dynamics

siControl and siMASTL MDA-MB-231 cells silenced for 48 h expressing mEmerald-paxillin were plated on ibidi plate (80826) coated with collagen (5 µg/ml) for 3 h before imaging. Fluorescent cells were then imaged live using a Marianas spinning disk imaging system with a Yokogawa CSU-W1 scanning unit on an inverted Zeiss Axio Observer Z1 microscope controlled by SlideBook 6 (Intelligent Imaging Innovations). Images were acquired every minute using a Photometrics Evolve, 10-MHz back-illuminated electron multiplying charge-coupled device (512 × 512 pixels) camera and 40× Zeiss long distance C-Apochromat water objective (NA 1.1).

To quantify focal adhesion dynamics, videos were preprocessed for brightness and background with ImageJ and further processed using the Focal Adhesion Analysis Server (http://faas.bme.unc.edu/; Berginski and Gomez, 2013) with the following analysis settings: minimum (min) adhesion size: 1; focal adhesion (FA) phase length: 5; and focal adhesion alignment index (FAAI): 3.

Western blot

Cells were washed with cold PBS, lysed with TX lysis buffer (TXLB; 50 mM Tris-HCl, pH 7.5, 150 mM NaCl, 0.5% Triton-X, 0.5% glycerol, 1% SDS, Complete protease inhibitor [Sigma-Aldrich], and phos-stop tablet [Sigma-Aldrich]), collected by scraping, and transferred into an Eppendorf tube. Samples were boiled for 5 min and sonicated. Protein concentrations were measured using DC Protein assay (Bio-Rad) according to the manufacturer's protocol, and protein concentrations were normalized by adding TXLB. SDS sample buffer was added on the samples, and samples were boiled for 5 min. To separate the proteins, samples with equal protein content were loaded on precast Tris-Glycine-eXtendet SDS-PAGE gels with a 4–20% gradient (Bio-Rad). The separated proteins were transferred onto nitrocellulose membranes (Bio-Rad) using the Trans-Blot Turbo Transfer System (Bio-Rad). Membranes were blocked with 5% milk powder in Tris-buffered saline with 0.1% Tween 20 (TBST) for 1 h at RT. Membranes were incubated in primary antibodies diluted in 5% milk in TBST at 4°C overnight. Membranes were washed three times with TBST and incubated with fluorophore-conjugated Odyssey secondary antibodies (LI-COR Biosciences) for 1 h at RT. Membranes were washed again and scanned with Odyssey infrared system (LI-COR Biosciences). Band intensities were analyzed using ImageJ.

Immunoprecipitation

MCF7 cells stably expressing EGFP, EGFP MASTL WT, or EGFP MASTL G44S were lysed in immunoprecipitation (IP)-lysis buffer (0.5% Triton X-100, 10 mM Pipes, pH 6.8, 150 mM NaCl, 150 mM sucrose, 3 mM $MgCl_2$, and complete protease and phosphatase inhibitors [Mediq; Roche]), cleared by centrifugation (13,226 *g*, 10 min, 4°C), and incubated with GFP-trap beads to pull down GFP proteins (gtak-20; Chromotek) for 1 h at 4°C. Complexes bound to the beads were isolated using 1,000 *g* 3-min centrifugation, washed three times with washing buffer (20 mM Tris-HCl, pH 7.5) 150 mM NaCl, and 1% NP-40; 500 µl), and eluted in sample buffer. Input and precipitate samples were analyzed by Western blotting.

Integrin activity

As a positive control, one culture plate was activated by adding 0.5 mM $MnCl_2$ to culture media for 1 h before collection. Cells were harvested with HyQTase, which was inactivated by addition of full media and washed with serum-free media.

For the fibronectin-binding assay, cells were pelleted with centrifugation at 200 *g* for 3 min and suspended into 100 µl of serum-free media. For sample reactions, 1:50 diluted FN647 (0.6 mg/ml, Alexa Fluor 647–conjugated FN7-10, a kind gift from Prof. R Fässler, Max Planck Institute of Biochemistry, Martinsried, Germany) was added. Positive control was supplemented with 0.5 mM $MnCl_2$ and negative control with 5 mM EDTA and preincubated for 10 min before addition of 1:50 diluted FN647 (0.6 mg/ml). All reactions were incubated 40 min at RT protected from light. Samples were washed two times with cold Tyrode's buffer (134 mM NaCl, 0.34 mM Na_2HPO_4, 2.9 mM KCl, 12 mM $NaHCO_3$, 20 mM Hepes, pH 7.0, 5 mM glucose, and 1 mM $CaCl_2$), fixed with 4% PFA, and washed before analysis.

For antibody labeling, cells were washed with cold PBS, fixed with 4% PFA for 15 min, and washed with Tyrode's buffer. Cells were then incubated with primary antibodies overnight at 4°C, washed, and incubated with secondary antibodies for 1 h at 4°C. After a final wash, cells were analyzed using a FACSCalibur (BD Biosciences) machine and Flowing software. The fibronectin-binding activation index was counted from the geometric mean fluorescence intensity (mGFI) using the formula $mGFI_{sample} - mGFI_{EDTA})/mGFI_{sample}$ and balanced to the signal of total integrin signal.

Cell cycle

Cells were detached with trypsin that was inactivated with full media. Cells were pelleted with centrifugation at 200 *g* for 3 min, washed with PBS, and fixed with 70% −20°C EtOH. EtOH was removed by centrifugation at 800 *g* for 4 min. Cells were washed with PBS supplemented with 2% FBS and resuspended into 200 µl of PBS. DNA was stained by adding 10 µl propidium iodide (1 mg/ml; Sigma) and 2 µl RNaseA (10 mg/ml) and incubated for 20 min. Cells were washed and analyzed using FACSCalibur (BD Biosciences) and FlowJo (BD Biosciences) using the Watson model.

Transcriptome analysis

Three biological replicates were prepared for control and MASTL#6 silenced cells for 48 h and two biological replicates for

Downloaded from http://rupress.org/jcb/article-pdf/219/6/e201906204/1615651/jcb_201906204.pdf by guest on 09 February 2026

24 h. RNA (500 ng) was amplified using Illumina TotalPrep RNA Amplification Kit (Applied Biosystems) continued by in vitro transcription reaction and biotinylation. The quality of the cRNA was validated with electrophoresis (Bioanalyzer; Agilent). Each cRNA (750 ng) was hybridized on HumanHT-12 v4 Expression Bead Chip microarray (Sentrix; Illumina) at 58°C for 19 h accordingly to the Illumina Whole-Genome Gene Expression Direct Hybridization Assay Guide protocol (part 11322355, rev. A). Arrays were scanned with Illumina Bead Array Reader (factor = 1.0, voltage of the photomultiplier tube = 520, filter = 100%) and results were processed with GenomeStudio v.2011.1; Gene Expression Module v.1.9.0.

The data were preprocessed using the Bioconductor lumi package (Du et al., 2008). More specifically, gene expression intensities were transformed using variance stabilizing transformation and normalized using the quantile normalization method (Lin et al., 2008). To reduce the number of false positives, probes that were determined as undetected (detection P value > 0.01) in all the samples were filtered out from further analysis. Out of the 47,321 probes on the array, 21,351 probes remained after the filtering (~45%). Differentially expressed genes were identified between the siRNA and control samples at 24-h and 48-h time points. Differential expression was determined using a data-driven statistical procedure that determines the test statistic by optimizing the reproducibility of the detections (Suomi et al., 2017). Genes with FDR < 0.05 were defined as changed.

Proteome analysis

For quantitative mass spectrometry (MS) analysis, SILAC cells were labeled by culturing them in DMEM without Arg/Lys (A14431-01), 200 µM L-glutamine, 100 U/ml penicillin streptomycin, 110 mg/l (1 mM) sodium pyruvate, and 10% 10 kD dialyzed serum (F0392; Sigma-Aldrich). The media for light labeling was supplemented with Arg 0 (84 mg/ml, A6969; Sigma-Aldrich) and Lys 0 (146 mg/ml, L8662; Sigma-Aldrich), and the media for heavy labeling was supplemented with Arg10 (CNLM-539-H; Cambridge Isotope Laboratories) and Lys8 (CNLM-291-H; Cambridge Isotope Laboratories). Incorporation of the isotopes was confirmed after six passages. siControl and siMASTL#6 silenced samples were prepared two times with light- and heavy-labeled cells, obtaining four experimental replicates. For each independent experiment, siControl and siMASTL-silenced samples were mixed using a label-swap replication strategy (i.e., siControl-light mixed with siMASTL silenced-heavy generates forward replicate 1; siMASTL silenced-light with siControl-heavy generates reverse replicate 1, etc.). 48 h after silencing the cells were lysed with 4% SDS, 100 mM DTT, and 100 mM Tris-HCl, pH 7.6, and boiled for 5 min at 95°C. Samples were sonicated, centrifuged at 13,000 *g* for 10 min at 4°C, and transferred into a clean tube.

Proteomic sample preparation

Proteins obtained from total cell lysates were precipitated in two steps using 24% and 10% solution of trichloroacetic acid. In both steps, pellets were incubated at 4°C for 10 min and centrifuged at 18,000 *g* for 5 min. Supernatants were carefully aspirated, and pellets were washed with water until the supernatant reached neutral pH. Pellets were reconstituted and digested, first using endoproteinase Lys-C (ratio 1:33 enzyme/lysate; Alpha Laboratories) for 1 h at RT (24°C) and then trypsin (ratio 1:33 enzyme/lysate; Promega) overnight at 35°C.

Offline HPLC fractionation

Protein digests were fractionated using high pH reverse-phase chromatography. A C18 column (150 × 2.1 mm inside diameter Kinetex EVO [5 µm, 100 Å]) was used with an HPLC system (LC 1260 Infinity II; Agilent). Modules were controlled by Chemstation rev 01.07 SR2. Solvent A (98% water, 2% acetonitrile) and solvent B (90% acetonitrile and 10% water) were adjusted to pH 10.0 using ammonium hydroxide. Samples were injected manually through a Rheodyne valve onto the reverse phase–high performance liquid chromatography (RP-HPLC) column equilibrated with 1% solvent B and kept at this percentage for 3 min. A two-step gradient was applied at a flow rate of 200 µl/min (from 1–25% B in 42 min and then from 25–43% B in 8 min) followed by an 8-min washing step at 100% solvent B and an 8-min re-equilibration step. Column eluate was monitored at 220 and 280 nm via a variable wavelength detector and collected using an Agilent 1260 infinity fraction collector. Column eluate was collected from 4 to 63 min and divided in 21 fractions.

Ultra-high performance liquid chromatography–MS/MS analysis

Fractionated tryptic digests were separated by nanoscale C18 reverse-phase liquid chromatography using an EASY-nLC II 1200 (Thermo Fisher Scientific) coupled to a Q-Exactive HF mass spectrometer (Thermo Fisher Scientific). Elution was performed using a binary gradient with buffer A (2% acetonitrile) and B (80% acetonitrile), both containing 0.1% formic acid. Samples were loaded into a 20 cm fused silica emitter (New Objective) packed in-house with ReproSil-Pur C18-AQ, 1.9 µm resin (Dr Maisch). Packed emitter was kept at 35°C by means of a column oven (Sonation) integrated into the nanoelectrospray ion source (Thermo Fisher Scientific).

Peptides were eluted at a flow rate of 300 nl/min using three different gradients optimized for different set of fractions as described previously (van der Reest et al., 2018). An Active Background Ion Reduction Device was used to decrease air contaminants signal level.

Data were acquired using Xcalibur software (Thermo Fisher Scientific), and acquisition was performed in positive-ion mode using data-dependent acquisition. A full scan (FT-MS) over mass range of 375–1,400 m/z was acquired at 60,000 resolution at 200 m/z, with a target value of 3,000,000 ions for a maximum injection time of 20 ms. Higher energy collisional dissociation fragmentation was performed on the 15 most intense ions, for a maximum injection time of 50 ms, or a target value of 50,000 ions. Multiply charged ions having intensity >12,000 counts were selected through a 1.5-m/z window and fragmented using normalized collision energy of 27. Former target ions selected for MS/MS were dynamically excluded for 25 s.

Proteomics data analysis

The MS raw data were processed with MaxQuant software (Cox and Mann, 2008) version 1.5.5.1 and searched with Andromeda

Downloaded from http://rupress.org/jcb/article-pdf/219/6/e201906204/1615651/jcb_201906204.pdf by guest on 09 February 2026

search engine (Cox et al., 2011), querying UniProt (UniProt Consortium, 2010; *Homo sapiens* [September 7, 2016; 92,939 entries]). For quantification, multiplicity was set to 2, and Arg0/Arg10 and Lys0/Lys8 were used for ratio calculation of SILAC-labeled peptides. First and main searches were performed with precursor mass tolerances of 20 ppm and 4.5 ppm, respectively, and MS/MS tolerance of 20 ppm. The minimum peptide length was set to six amino acids, and specificity for trypsin cleavage was required, allowing up to two missed cleavage sites. Methionine oxidation and N-terminal acetylation were specified as variable modifications and cysteine carbamidomethylation as fixed modification. The peptide and protein FDR was set to 1%.

MaxQuant output was further processed and analyzed using Perseus software version 1.5.5.4. Quantification was done using the ProteinGroups.txt file, reverse and potential contaminant flagged proteins were removed, and at least one uniquely assigned peptide and a minimum ratio count of 2 were required for a protein to be quantified.

To identify regulated proteins, the two-sided significance B algorithm (Cox and Mann, 2008) with a threshold value of 0.05 (Benjamini–Hochberg FDR used for truncation) was applied to each replicate sample.

RT-PCR

RNA was isolated using the Nucleospin RNA kit (BioTop) followed by DNase digestion with DNaseI Amplification Grade kit (Invitrogen). RNA was processed to cDNA using high capacity cDNA Reverse Transcription Kit (Thermo Fisher Scientific).

Micropatterns and stress fiber analysis

Coverglasses were coated with poly-L-lysine–grafted polyethylene glycol to prevent protein binding. Micropatterns were produced by exposing the coated glasses to UV light through a micropatterned microplate to break poly-L-lysine–grafted polyethylene glycol bonds and enable proteins to bind on the micropatterns (Azioune et al., 2009). The micropatterns were coated with 5 µg/ml collagen overnight at 4°C and washed with PBS, and cells were plated on micropatterned coverslips for 2 h. Cells were fixed with 4% PFA, washed with PBS, permeabilized with 0.2% Triton in PBS, stained with pMLC antibody overnight at 4°C, and then washed with PBS and incubated with Alexa Fluor 488 secondary antibody, Phalloidin Atto 647N (F-actin), and DAPI (nucleus). Stress fibers were analyzed from images stained with Phalloidin-Atto. The number of stress fibers was analyzed by visual scoring and subdivided into three categories: low, no obvious stress fibers; moderate, one to four stress fibers; and high, five or more stress fibers. The width of the lamellipodium was measured from the widest point of the lamellipodium and divided into three categories: narrow, 0–1.2 µm; moderate, 1.2–2 µm; and wide, >2 µm.

Migration assay

siRNA-treated and/or transfected MDA-MB-231 cells were plated on a 24-well plate in full growth media. The wells were coated with 5 µg/ml collagen overnight at 4°C before the experiment. Cells were imaged every 10 min for 10 h using a Nikon Eclipse Ti-E widefield microscope, Hamamatsu Orca C13440 Flash 4.0 ERG (b/w) sCMOS camera, and 20× Plan Apo lambda, NA 0.75, WD 1,000 µm objective (for silenced cells) or 20× Nikon CFI S Plan Fluor ELWD, NA 0.45, WD 8,200 µm (for silenced and transfected cells). Cells were kept in full media and normal growth conditions (37°C, 5% CO_2) during imaging. To quantify cell migration, cells were tracked with National Institutes of Health (NIH) ImageJ Manual Tracking plug-in and analyzed with NIH ImageJ Chemotaxis tool.

Inverted invasions

Inverted invasion assays were performed as previously described (Jacquemet et al., 2016). Briefly, 200 µl collagen I (5 mg/ml; #5074, PureCol EZ Gel; Advanced BioMatrix) spiked with fibronectin (25 µg/ml; #341631; Millipore) was allowed to polymerize inside transwell inserts (8 µm ThinCert; Greiner Bio-One) for 1 h at 37°C. MDA-MB-231 cells were silenced with siControl, siMASTL #6, siMASTL #11, siMRTF-A #1, and siMRTF-A #2 in serum-free media overnight, as above. The transwells were then inverted, and 10^5 cells/insert were seeded onto the opposite face of the filter and allowed to incubate upside down for a further 3 h at 37°C. Inserts were then washed with PBS before placement in 1 ml serum-free medium/24-well well. To establish a chemotactic gradient, 300 µl media supplemented with 10% FBS was placed in the top of the transwell insert. After 96 h, invading cells were fixed in 4% PFA with 0.5% (vol/vol) Triton-X-100 at RT for 2 h. Invasions were then stained overnight at 4°C using Alexa Fluor 488 phalloidin (1:50, A12379; Life Technologies). These were then washed three times using PBS and imaged on a confocal microscope (LSM880; Zeiss), capturing serial optical sections every 15 µm with a 40× objective (NA 1.2 immersion, Plan-Apochromat). Invasion was quantified with ImageJ (NIH) using the area calculator function, comparing the area covered by cells that had invaded ≥45 µm, as a percentage of the area of all cells within the matrix.

For immunofluorescence staining, fixed invasions were subsequently removed from the transwell inserts and cut in half before blocking with 5% BSA and incubation with MRTF-A primary antibody overnight at 4°C. These were then washed with PBS and incubated for 1 h at RT with anti-mouse-568 and Hoechst 33342 (5 µg/ml, H3570; Invitrogen). After further washing, samples were imaged on a confocal microscope (LSM880; Zeiss), capturing serial optical sections every 1–2 µm with a 40× objective (NA 1.2 immersion, Plan-Apochromat). Collagen within the inverted invasion matrices was visualized by reflectance confocal microscopy using the 633-nm laser line. Cell shape was then assessed in ImageJ (NIH) with the shape descriptor measurement, roundness. The MRTF-A nuclear-to-cytoplasmic ratio in invasive MDA-MB-231 cells in 3D collagen matrices was assessed by measuring the integrated density of MRTF-A staining in regions masked with Hoechst 33342 and phalloidin-488 and then calculating the ratio of staining intensity between these two cellular compartments.

FLIP

MCF7 cells were silenced overnight with siControl and siMASTL #11, as above, before transfection with pInd20-MTRF-A-EGFP overnight in serum-free media, as above, in the presence of 1 µg/ml

Downloaded from http://rupress.org/jcb/article-pdf/219/6/e201906204/1615651/jcb_201906204.pdf by guest on 09 February 2026

doxycycline. FLIP experiments were conducted on a confocal microscope (LSM880; Zeiss) with a 40× objective (NA 1.2 immersion, Plan-Apochromat) using cells that had been incubated with Sir-DNA (1:2,000, CY-SC007; Cytoskeleton) for 1 h. Bleaching was then performed after addition of 10% FBS for 10 min using the 488-nm laser line in a 75 × 125 µm region of the cytoplasm and surroundings, excluding the nucleus, every 20 s for at least 12 min, acquiring an image of the cell after each bleach. A ratio for MRTF-A localization was measured by first making a nuclear mask using the Sir-DNA channel and then measuring the integrated density of the fluorescent MRTF-A signal in the nuclear region of interest at each time point using ImageJ.

Orientation analysis

β-Catenin junction orientation analysis was performed on confocal images using the OrientationJ plugin for ImageJ (NIH; https://www.ncbi.nlm.nih.gov/pubmed/21744269). This was done by computing the structure tensors within each input image using a cubic spline interpolation, which assesses the local orientation and isotropic properties of the pixels. The local predominant orientation of these tensors (measured in degrees) was then peak aligned and the frequency of junction alignment calculated across the 30° spanning the peak alignment.

F-actin/G-actin fractionation

MCF10A cells were treated with siRNAs for 48 h or with 0.1 µM jasplakinolide (J4580; Sigma-Aldrich) or DMSO (control) for 30 min. Cells were washed twice with PBS on ice and lysed with 750 µl actin lysis buffer (0.5% Triton-X, 20 mM Hepes, pH 7.9, 50 mM NaCl, 1 mM EDTA, and EDTA-free protease inhibitor cocktail tablet [Roche] in PBS) on ice for 15 min (Grosse et al., 2003; Posern et al., 2002). Cells were collected by scraping and fractionated by ultracentrifugation at 100,000 *g* for 1 h at 4°C. The supernatant (G-actin fraction) was collected and mixed with SDS-PAGE loading buffer, whereas the pellet (F-actin fraction) was resuspended with 750 µl actin lysis buffer mixed with SDS-PAGE loading buffer. Equal amounts of fractions were separated on SDS-PAGE followed by immunoblotting with indicated antibodies.

qPCR

RNA was isolated from siRNA treated (72 h) MCF10A cells by using Trizol reagent (Peqlab) according to the manufacturer's instructions followed by reverse transcription done by using RevertAid Reverse transcription (Thermo Fisher Scientific). Obtained cDNA was quantified using SYBR green Master Mix (Bio-Rad) with real-time qPCR on a Real Time Quantitative Thermal Cycle (Bio-Rad).

SRF luciferase assay

To assess SRF activity, we used a MCF10A cell line stably expressing MRTF-SRF–specific promoter 3Da.luc linked to GFP (Hinojosa et al., 2017). These cells were transfected with control, MASTL#6, and SRF siRNAs. After 48 h, cells were serum deprived for 24 h followed by serum stimulation with 0% (control) or 20% horse serum for 7 h. The amount of firefly was measured luminometrically for each condition. Alternatively, MRTF/SRF activity was determined as described previously (Kreßner et al., 2013) using p3DA.luc (firefly luciferase) and pRL-TK (Renilla luciferase control) reporter plasmids transiently transfected to MCF7 cells with EGFP or EGFP-MASTL plasmids, as indicated. After transfection, cells were maintained in 0.5% FBS for 17 h before analysis and stimulated with 20% FBS for 7 h. The amount of firefly relative to Renilla was measured luminometrically for each condition.

MRTF-A translocation assay

MCF10A cells stably expressing pIND20-MRTF-A-GFP were transiently transfected with siMASTL#6 or control siRNAs. After 48 h silencing and 24 h before live-cell imaging, cells were simultaneously serum-deprived and stimulated with 333 ng/ml doxycycline to induce MRTF-A-GFP expression. Serum stimulation was performed by adding 20% serum to the cells under a confocal microscope LSM 800 (Zeiss), and cells were imaged in a CO_2-humidified incubation chamber every 10 s to study MRTF-A nuclear translocation. Alternatively, MCF10A cells were plated on glass-bottom plates (MatTek) for 24 h and transfected with EGFP or EGFP-MASTL plasmids in serum-free medium. After 24 h, 20% horse serum was added, and cells were fixed with 4% PFA 0, 2, or 5 min after adding serum. Next, the cells were permeabilized with 0.1% Triton in PBS and stained with MRTF-A antibody overnight at 4°C, washed with PBS, and incubated with Alexa Fluor 555 secondary antibody, Phalloidin-Atto 647N (F-actin), and DAPI (nucleus). The samples were imaged with the Marianas spinning disk imaging system with a Yokogawa CSU-W1 scanning unit on an inverted Zeiss Axio Observer Z1 microscope controlled by SlideBook 6 (Intelligent Imaging Innovations) using an Orca Flash 4 sCMOS camera (2,048 × 2,048; Hamamatsu Photonics) and 20× (NA 0.8 air, Plan Apo, DIC; Zeiss) objective.

Quantification and statistical analysis

Detailed statistical analyses used for individual experiments are listed in Table S1. GraphPad Prism version 6.05 for Windows (GraphPad Software) was used to determine the P values and perform statistical analysis. An unpaired *t* test with Gaussian distribution was used, and mean with SD values are presented in all figures, except for stress fiber quantification (Fig. 5, B and C), where the Fisher's exact test was applied; and accumulative distance for migration (Fig. 6 C), where Welch's correction was performed. The result was defined to be significant if the P value was < 0.05. The exact P values < 0.05 are marked in each figure. Higher P values are marked not significant in the figures, and the exact P values are provided in Table S1.

Data and software availability

The transcriptome data are available in the Gene Expression Omnibus (GEO), accession no. GSE131833. The mass spectrometry proteomics data have been deposited to the ProteomeXchange Consortium via the PRIDE (Perez-Riverol et al., 2019) partner repository with the dataset identifier PXD013757.

The proteome data are available in PRIDE. The raw files and the MaxQuant search results files have been deposited as partial

Downloaded from http://rupress.org/jcb/article-pdf/219/6/e201906204/1615651/jcb_201906204.pdf by guest on 09 February 2026

submission to the ProteomeXchange Consortium via the PRIDE partner repository (Perez-Riverol et al., 2019) with the dataset identifier PXD013757.

Online supplemental material

Fig. S1 shows that MASTL depletion promotes MDA-MB-231 cell spreading and attachment on fibronectin and collagen (related to Figs. 1 and 2). Fig. S2 shows MASTL protein levels in one normal breast and two breast cancer cell lines and that MASTL silencing promotes cell spreading in MCF7 breast cancer cells and MASTL silencing does not affect focal adhesion size, integrin activity, or cell cycle in MDA-MB-231 cells (related to Fig. 2). Fig. S3 confirms MASTL silencing with Western blot and RT-PCR (for transcriptome and proteome experiments related to Fig. 4). Fig. S4 contains Western blot and/or immunofluorescence anlysi of GEF-H1 and Tpm4.2 expression in MCF10A and MDA-MB-231 cells after MASTL silencing with an additoinal siRNA. Moreover, transient GEF-H1 expression after MASTL silencing does not rescue cell migration (related to Fig. 5). Fig. S5 shows that MASTL depletion reduces vinculin-positive focal adhesion size, vinculin is present in cell–cell junctions, overexpression of MASTL-E167D cannot induce SRF activity, and that MASTL silencing does not affect the F-actin/G-actin ratio (related to Fig. 8). Table S1 contains the statistics related to all figures. Table S2 shows the Illumina transcriptome data of MASTL-silenced cells (related to Fig. 3). Table S3 contains the SILAC proteome data of MASTL-silenced cells (related to Fig. 3). Video 1 is a bright-field time-lapse movie of siControl MDA-MB-231 cells migrating on collagen (related to Fig. 7). Video 2 is a bright-field time-lapse movie of siMASTL MDA-MB-231 cells migrating on collagen (related to Fig. 7). Video 3 is a time-lapse movie of focal adhesion kinetics in mEmerald-paxillin–labeled siControl and siMASTL MDA-MB-231 cells.

Acknowledgments

We thank J. Siivonen and P. Laasola for technical assistance and M. Miihkinen for generating the E167D mutation. H. Hamidi is acknowledged for editing the manuscript. The Ivaska laboratory is acknowledged for lively discussions and critical feedback on the manuscript. We thank Prof. P. Gunning for providing reagents. The Cell Imaging and Cytometry core facility (Turku Bioscience Centre, University of Turku and Åbo Akademi University and Biocenter, Finland); EuroBioimaging node in Turku, Finnish Functional Genomics Centre (Turku Bioscience Centre, University of Turku and Åbo Akademi University); and the Mass Spectrometry Unit of the Beatson Institute for Cancer Research are acknowledged for services, instrumentation, and expertise.

This study was supported by the Academy of Finland (E. Närvä grant 297079 and J. Ivaska grant 312517), the Academy of Finland CoE for Translational Cancer Biology (J. Ivaska), the European Research Council CoG grant 615258 (J. Ivaska), the Sigrid Juselius Foundation (J. Ivaska), the Finnish Cancer Organization (J. Ivaska and E. Närvä), Cancer Research UK (grants A17196 and A12935 to S. Lilla and S. Zanivan), and the Wilhelm-Sander Foundation (grant 2013.149.2 to R. Grosse). M.E. Taskinen has been supported by the University of Turku Doctoral Program for Molecular Medicine. J.R.W. Conway has been supported by the European Union's Horizon 2020 research and innovation program under Marie Sklodowska-Curie grant agreement 841973. We also acknowledge EMBO for a short-term fellowship (E. Närvä).

The authors declare no competing financial interests.

Author contributions: Conceptualization, E. Närvä, M.E. Taskinen, and J. Ivaska; Methodology, M.E. Taskinen, E. Närvä, J.R.W. Conway, L. Soto Hinojosa, S. Lilla, A. Mai, and N. De Franceschi; Formal Analysis, E. Närvä, M.E. Taskinen, J.R.W. Conway, S. Lilla, L.L. Elo, and L. Soto Hinojosa; Writing – Original Draft, E. Närvä, M.E. Taskinen, and J. Ivaska; Writing – Editing, E. Närvä, M.E. Taskinen, J.R.W. Conway, and J. Ivaska; Visualization, E. Närvä, M.E. Taskinen, and J.R.W. Conway; Supervision, J. Ivaska, J.C. Norman, S. Zanivan, and R. Grosse; Funding Acquisition, J. Ivaska.

Submitted: 28 June 2019
Revised: 3 February 2020
Accepted: 11 March 2020

References

Aijaz, S., F. D'Atri, S. Citi, M.S. Balda, and K. Matter. 2005. Binding of GEF-H1 to the tight junction-associated adaptor cingulin results in inhibition of Rho signaling and G1/S phase transition. *Dev. Cell.* 8:777–786. https://doi.org/10.1016/j.devcel.2005.03.003

Álvarez-Fernández, M., M. Sanz-Flores, B. Sanz-Castillo, M. Salazar-Roa, D. Partida, E. Zapatero-Solana, H.R. Ali, E. Manchado, S. Lowe, T. VanArsdale, et al. 2018. Therapeutic relevance of the PP2A-B55 inhibitory kinase MASTL/Greatwall in breast cancer. *Cell Death Differ.* 25:828–840.

Ammarah, U., A. Kumar, R. Pal, N.C. Bal, and G. Misra. 2018. Identification of new inhibitors against human Great wall kinase using in silico approaches. *Sci. Rep.* 8:4894. https://doi.org/10.1038/s41598-018-23246-0

Azioune, A., M. Storch, M. Bornens, M. Théry, and M. Piel. 2009. Simple and rapid process for single cell micro-patterning. *Lab Chip.* 9:1640–1642. https://doi.org/10.1039/b821581m

Baarlink, C., H. Wang, and R. Grosse. 2013. Nuclear actin network assembly by formins regulates the SRF coactivator MAL. *Science.* 340:864–867. https://doi.org/10.1126/science.1235038

Berginski, M.E., and S.M. Gomez. 2013. The Focal Adhesion Analysis Server: a web tool for analyzing focal adhesion dynamics. *F1000 Res.* 2:68. https://doi.org/10.12688/f1000research.2-68.v1

Birkenfeld, J., P. Nalbant, S.-H. Yoon, and G.M. Bokoch. 2008. Cellular functions of GEF-H1, a microtubule-regulated Rho-GEF: is altered GEF-H1 activity a crucial determinant of disease pathogenesis? *Trends Cell Biol.* 18:210–219. https://doi.org/10.1016/j.tcb.2008.02.006

Carreno, S., I. Kouranti, E.S. Glusman, M.T. Fuller, A. Echard, and F. Payre. 2008. Moesin and its activating kinase Slik are required for cortical stability and microtubule organization in mitotic cells. *J. Cell Biol.* 180:739–746. https://doi.org/10.1083/jcb.200709161

Cetti, E., T. Di Marco, G. Mauro, M. Mazzoni, D. Lecis, E. Minna, L. Gioiosa, S. Brich, S. Pagliardini, M.G. Borrello, et al. 2019. Mitosis perturbation by MASTL depletion impairs the viability of thyroid tumor cells. *Cancer Lett.* 442:362–372. https://doi.org/10.1016/j.canlet.2018.11.010

Chaigne, A., C. Campillo, N.S. Gov, R. Voituriez, J. Azoury, C. Umaña-Diaz, M. Almonacid, I. Queguiner, P. Nassoy, C. Sykes, et al. 2013. A soft cortex is essential for asymmetric spindle positioning in mouse oocytes. *Nat. Cell Biol.* 15:958–966. https://doi.org/10.1038/ncb2799

Charrasse, S., A. Gharbi-Ayachi, A. Burgess, J. Vera, K. Hached, P. Raynaud, E. Schwob, T. Lorca, and A. Castro. 2017. Ensa controls S-phase length by modulating Treslin levels. *Nat. Commun.* 8:206. https://doi.org/10.1038/s41467-017-00339-4

Chiang, H.-S., Y. Zhao, J.-H. Song, S. Liu, N. Wang, C. Terhorst, A.H. Sharpe, M. Basavappa, K.L. Jeffrey, and H.-C. Reinecker. 2014. GEF-H1 controls microtubule-dependent sensing of nucleic acids for antiviral host defenses. *Nat. Immunol.* 15:63–71. https://doi.org/10.1038/ni.2766

Downloaded from http://rupress.org/jcb/article-pdf/219/6/e201906204/1615651/jcb_201906204.pdf by guest on 09 February 2026

Cox, J., and M. Mann. 2008. MaxQuant enables high peptide identification rates, individualized p.p.b.-range mass accuracies and proteome-wide protein quantification. *Nat. Biotechnol.* 26:1367–1372. https://doi.org/10.1038/nbt.1511

Cox, J., N. Neuhauser, A. Michalski, R.A. Scheltema, J.V. Olsen, and M. Mann. 2011. Andromeda: a peptide search engine integrated into the MaxQuant environment. *J. Proteome Res.* 10:1794–1805. https://doi.org/10.1021/pr101065j

Cullis, J., D. Meiri, M.J. Sandi, N. Radulovich, O.A. Kent, M. Medrano, D. Mokady, J. Normand, J. Larose, R. Marcotte, et al. 2014. The RhoGEF GEF-H1 is required for oncogenic RAS signaling via KSR-1. *Cancer Cell.* 25:181–195. https://doi.org/10.1016/j.ccr.2014.01.025

Du, P., W.A. Kibbe, and S.M. Lin. 2008. lumi: a pipeline for processing Illumina microarray. *Bioinformatics.* 24:1547–1548. https://doi.org/10.1093/bioinformatics/btn224

Esnault, C., A. Stewart, F. Gualdrini, P. East, S. Horswell, N. Matthews, and R. Treisman. 2014. Rho-actin signaling to the MRTF coactivators dominates the immediate transcriptional response to serum in fibroblasts. *Genes Dev.* 28:943–958. https://doi.org/10.1101/gad.239327.114

Gandalovičová, A., D. Rosel, M. Fernandes, P. Veselý, P. Heneberg, V. Čermák, L. Petruželka, S. Kumar, V. Sanz-Moreno, and J. Brábek. 2017. Migrastatics-Anti-metastatic and Anti-invasion Drugs: Promises and Challenges. *Trends Cancer.* 3:391–406. https://doi.org/10.1016/j.trecan.2017.04.008

Gao, Y., E. Smith, E. Ker, P. Campbell, E.C. Cheng, S. Zou, S. Lin, L. Wang, S. Halene, and D.S. Krause. 2012. Role of RhoA-specific guanine exchange factors in regulation of endomitosis in megakaryocytes. *Dev. Cell.* 22: 573–584. https://doi.org/10.1016/j.devcel.2011.12.019

Gateva, G., E. Kremneva, T. Reindl, T. Kotila, K. Kogan, L. Gressin, P.W. Gunning, D.J. Manstein, A. Michelot, and P. Lappalainen. 2017. Tropomyosin Isoforms Specify Functionally Distinct Actin Filament Populations In Vitro. *Curr. Biol.* 27:705–713. https://doi.org/10.1016/j.cub.2017.01.018

Gau, D., and P. Roy. 2018. SRF'ing and SAP'ing - the role of MRTF proteins in cell migration. *J. Cell Sci.* 131:jcs218222. https://doi.org/10.1242/jcs.218222

Geeves, M.A., S.E. Hitchcock-DeGregori, and P.W. Gunning. 2015. A systematic nomenclature for mammalian tropomyosin isoforms. *J. Muscle Res. Cell Motil.* 36:147–153. https://doi.org/10.1007/s10974-014-9389-6

Grosse, R., J.W. Copeland, T.P. Newsome, M. Way, and R. Treisman. 2003. A role for VASP in RhoA-Diaphanous signalling to actin dynamics and SRF activity. *EMBO J.* 22:3050–3061. https://doi.org/10.1093/emboj/cdg287

Guettler, S., M.K. Vartiainen, F. Miralles, B. Larijani, and R. Treisman. 2008. RPEL motifs link the serum response factor cofactor MAL but not myocardin to Rho signaling via actin binding. *Mol. Cell. Biol.* 28:732–742. https://doi.org/10.1128/MCB.01623-07

Guilluy, C., V. Swaminathan, R. Garcia-Mata, E.T. O'Brien, R. Superfine, and K. Burridge. 2011. The Rho GEFs LARG and GEF-H1 regulate the mechanical response to force on integrins. *Nat. Cell Biol.* 13:722–727. https://doi.org/10.1038/ncb2254

Hamidi, H., and J. Ivaska. 2018. Every step of the way: integrins in cancer progression and metastasis. *Nat. Rev. Cancer.* 18:533–548. https://doi.org/10.1038/s41568-018-0038-z

Hinojosa, L.S., M. Holst, C. Baarlink, and R. Grosse. 2017. MRTF transcription and Ezrin-dependent plasma membrane blebbing are required for entotic invasion. *J. Cell Biol.* 216:3087–3095. https://doi.org/10.1083/jcb.201702010

Hirata, H., H. Tatsumi, and M. Sokabe. 2008. Mechanical forces facilitate actin polymerization at focal adhesions in a zyxin-dependent manner. *J. Cell Sci.* 121:2795–2804. https://doi.org/10.1242/jcs.030320

Hotulainen, P., and P. Lappalainen. 2006. Stress fibers are generated by two distinct actin assembly mechanisms in motile cells. *J. Cell Biol.* 173: 383–394. https://doi.org/10.1083/jcb.200511093

Hurtado, B., M. Trakala, P. Ximénez-Embún, A. El Bakkali, D. Partida, B. Sanz-Castillo, M. Álvarez-Fernández, M. Maroto, R. Sánchez-Martínez, L. Martínez, et al. 2018. Thrombocytopenia-associated mutations in Ser/Thr kinase MASTL deregulate actin cytoskeletal dynamics in platelets. *J. Clin. Invest.* 128:5351–5367. https://doi.org/10.1172/JCI121876

Itoh, K., O. Ossipova, and S.Y. Sokol. 2014. GEF-H1 functions in apical constriction and cell intercalations and is essential for vertebrate neural tube closure. *J. Cell Sci.* 127:2542–2553. https://doi.org/10.1242/jcs.146811

Jacquemet, G., H. Baghirov, M. Georgiadou, H. Sihto, E. Peuhu, P. Cettour-Janet, T. He, M. Perälä, P. Kronqvist, H. Joensuu, and J. Ivaska. 2016. L-type calcium channels regulate filopodia stability and cancer cell invasion downstream of integrin signalling. *Nat. Commun.* 7:13297. https://doi.org/10.1038/ncomms13297

Kopf, A., J. Renkawitz, R. Hauschild, I. Girkontaite, K. Tedford, J. Merrin, O. Thorn-Seshold, D. Trauner, H. Häcker, K.-D. Fischer, et al 2019. Microtubules coordinate protrusion-retraction dynamics in migrating dendritic cells. *bioRxiv.* doi: https://doi.org/ (Preprint posted April 15, 2019)https://doi.org/10.1101/609420

Kreßner, C., P. Nollau, R. Grosse, and D.T. Brandt. 2013. Functional interaction of SCAI with the SWI/SNF complex for transcription and tumor cell invasion. *PLoS ONE.* 8(8):e69947. . https://doi.org/10.1371/journal.pone.0069947

Kunda, P., A.E. Pelling, T. Liu, and B. Baum. 2008. Moesin controls cortical rigidity, cell rounding, and spindle morphogenesis during mitosis. *Curr. Biol.* 18:91–101. https://doi.org/10.1016/j.cub.2007.12.051

Lin, S.M., P. Du, W. Huber, and W.A. Kibbe. 2008. Model-based variance-stabilizing transformation for Illumina microarray data. *Nucleic Acids Res.* 36:e11. https://doi.org/10.1093/nar/gkm1075

Ly, D.L., F. Waheed, M. Lodyga, P. Speight, A. Masszi, H. Nakano, M. Hersom, S.F. Pedersen, K. Szászi, and A. Kapus. 2013. Hyperosmotic stress regulates the distribution and stability of myocardin-related transcription factor, a key modulator of the cytoskeleton. *Am. J. Physiol. Cell Physiol.* 304:C115–C127. https://doi.org/10.1152/ajpcell.00290.2012

Marzec, K., and A. Burgess. 2018. The Oncogenic Functions of MASTL Kinase. *Front. Cell Dev. Biol.* 6:162. https://doi.org/10.3389/fcell.2018.00162

Medeiros, N.A., D.T. Burnette, and P. Forscher. 2006. Myosin II functions in actin-bundle turnover in neuronal growth cones. *Nat. Cell Biol.* 8: 215–226. https://doi.org/10.1038/ncb1367

Medjkane, S., C. Perez-Sanchez, C. Gaggioli, E. Sahai, and R. Treisman. 2009. Myocardin-related transcription factors and SRF are required for cytoskeletal dynamics and experimental metastasis. *Nat. Cell Biol.* 11: 257–268. https://doi.org/10.1038/ncb1833

Mendes Pinto, I., B. Rubinstein, and R. Li. 2013. Force to divide: structural and mechanical requirements for actomyosin ring contraction. *Biophys. J.* 105:547–554. https://doi.org/10.1016/j.bpj.2013.06.033

Miralles, F., G. Posern, A.-I. Zaromytidou, and R. Treisman. 2003. Actin dynamics control SRF activity by regulation of its coactivator MAL. *Cell.* 113:329–342. https://doi.org/10.1016/S0092-8674(03)00278-2

Murrell, M., P.W. Oakes, M. Lenz, and M.L. Gardel. 2015. Forcing cells into shape: the mechanics of actomyosin contractility. *Nat. Rev. Mol. Cell Biol.* 16:486–498. https://doi.org/10.1038/nrm4012

Nagel, R., M. Stigter-van Walsum, M. Buijze, J. van den Berg, I.H. van der Meulen, J. Hodzic, S.R. Piersma, T.V. Pham, C.R. Jiménez, V.W. van Beusechem, and R.H. Brakenhoff. 2015. Genome-wide siRNA Screen Identifies the Radiosensitizing Effect of Downregulation of MASTL and FOXM1 in NSCLC. *Mol. Cancer Ther.* 14:1434–1444. https://doi.org/10.1158/1535-7163.MCT-14-0846

Olson, E.N., and A. Nordheim. 2010. Linking actin dynamics and gene transcription to drive cellular motile functions. *Nat. Rev. Mol. Cell Biol.* 11: 353–365. https://doi.org/10.1038/nrm2890

Paszek, M.J., C.C. DuFort, M.G. Rubashkin, M.W. Davidson, K.S. Thorn, J.T. Liphardt, and V.M. Weaver. 2012. Scanning angle interference microscopy reveals cell dynamics at the nanoscale. *Nat. Methods.* 9(8): 825–827. . https://doi.org/10.1038/nmeth.2077

Pathak, R., V.D. Delorme-Walker, M.C. Howell, A.N. Anselmo, M.A. White, G.M. Bokoch, and C. Dermardirossian. 2012. The microtubule-associated Rho activating factor GEF-H1 interacts with exocyst complex to regulate vesicle traffic. *Dev. Cell.* 23:397–411. https://doi.org/10.1016/j.devcel.2012.06.014

Perez-Riverol, Y., A. Csordas, J. Bai, M. Bernal-Llinares, S. Hewapathirana, D.J. Kundu, A. Inuganti, J. Griss, G. Mayer, M. Eisenacher, et al. 2019. The PRIDE database and related tools and resources in 2019: improving support for quantification data. *Nucleic Acids Res.* 47(D1):D442–D450. https://doi.org/10.1093/nar/gky1106

Pollard, T.D. 2010. Mechanics of cytokinesis in eukaryotes. *Curr. Opin. Cell Biol.* 22:50–56. https://doi.org/10.1016/j.ceb.2009.11.010

Pollard, T.D., and J.A. Cooper. 2009. Actin, a central player in cell shape and movement. *Science.* 326:1208–1212. https://doi.org/10.1126/science.1175862

Posern, G., A. Sotiropoulos, and R. Treisman. 2002. Mutant actins demonstrate a role for unpolymerized actin in control of transcription by serum response factor. *Mol. Biol. Cell.* 13:4167–4178. https://doi.org/10.1091/mbc.02-05-0068

Rogers, S., R.A. McCloy, B.L. Parker, D. Gallego-Ortega, A.M.K. Law, V.T. Chin, J.R.W. Conway, D. Fey, E.K.A. Millar, S. O'Toole, et al. 2018. MASTL overexpression promotes chromosome instability and metastasis in breast cancer. *Oncogene.* 37:4518–4533. https://doi.org/10.1038/s41388-018-0295-z

Rottner, K., J. Faix, S. Bogdan, S. Linder, and E. Kerkhoff. 2017. Actin assembly mechanisms at a glance. *J. Cell Sci.* 130:3427–3435. https://doi.org/10.1242/jcs.206433

Downloaded from http://rupress.org/jcb/article-pdf/219/6/e201906204/1615651/jcb_201906204.pdf by guest on 09 February 2026

Schevzov, G., S.P. Whittaker, T. Fath, J.J. Lin, and P.W. Gunning. 2011. Tropomyosin isoforms and reagents. *Bioarchitecture*. 1(4):135–164. . https://doi.org/10.4161/bioa.1.4.17897

Suomi, T., F. Seyednasrollah, M.K. Jaakkola, T. Faux, and L.L. Elo. 2017. ROTS: An R package for reproducibility-optimized statistical testing. *PLOS Comput. Biol.* 13:e1005562. https://doi.org/10.1371/journal.pcbi.1005562

Théry, M., V. Racine, A. Pépin, M. Piel, Y. Chen, J.-B. Sibarita, and M. Bornens. 2005. The extracellular matrix guides the orientation of the cell division axis. *Nat. Cell Biol.* 7:947–953. https://doi.org/10.1038/ncb1307

Tojkander, S., G. Gateva, G. Schevzov, P. Hotulainen, P. Naumanen, C. Martin, P.W. Gunning, and P. Lappalainen. 2011. A molecular pathway for myosin II recruitment to stress fibers. *Curr. Biol.* 21:539–550. https://doi.org/10.1016/j.cub.2011.03.007

UniProt Consortium. 2010. The Universal Protein Resource (UniProt) in 2010. *Nucleic Acids Res.* 38:D142–D148.

van der Reest, J., S. Lilla, L. Zheng, S. Zanivan, and E. Gottlieb. 2018. Proteome-wide analysis of cysteine oxidation reveals metabolic sensitivity to redox stress. *Nat. Commun.* 9:1581. https://doi.org/10.1038/s41467-018-04003-3

Vartiainen, M.K., S. Guettler, B. Larijani, and R. Treisman. 2007. Nuclear actin regulates dynamic subcellular localization and activity of the SRF cofactor MAL. *Science.* 316:1749–1752. https://doi.org/10.1126/science.1141084

Vera, J., L. Lartigue, S. Vigneron, G. Gadea, V. Gire, M. Del Rio, I. Soubeyran, F. Chibon, T. Lorca, and A. Castro. 2015. Greatwall promotes cell transformation by hyperactivating AKT in human malignancies. *eLife.* 4:e10115. https://doi.org/10.7554/eLife.10115

Vigneron, S., P. Robert, K. Hached, L. Sundermann, S. Charrasse, J.-C. Labbé, A. Castro, and T. Lorca. 2016. The master Greatwall kinase, a critical regulator of mitosis and meiosis. *Int. J. Dev. Biol.* 60:245–254. https://doi.org/10.1387/ijdb.160155tl

Voets, E., and R.M.F. Wolthuis. 2010. MASTL is the human orthologue of Greatwall kinase that facilitates mitotic entry, anaphase and cytokinesis. *Cell Cycle.* 9:3591–3601. https://doi.org/10.4161/cc.9.17.12832

Wang, P., M. Larouche, K. Normandin, D. Kachaner, H. Mehsen, G. Emery, and V. Archambault. 2016. Spatial regulation of greatwall by Cdk1 and PP2A-Tws in the cell cycle. *Cell Cycle.* 15:528–539. https://doi.org/10.1080/15384101.2015.1127476

Wang, H., J. Wang, J. Yang, X. Yang, J. He, R. Wang, S. Liu, L. Zhou, and L. Ma. 2017. Guanine nucleotide exchange factor -H1 promotes inflammatory cytokine production and intracellular mycobacterial elimination in macrophages. *Cell Cycle.* 16:1695–1704. https://doi.org/10.1080/15384101.2017.1347739

Wilson, C.A., M.A. Tsuchida, G.M. Allen, E.L. Barnhart, K.T. Applegate, P.T. Yam, L. Ji, K. Keren, G. Danuser, and J.A. Theriot. 2010. Myosin II contributes to cell-scale actin network treadmilling through network disassembly. *Nature.* 465:373–377. https://doi.org/10.1038/nature08994

Wong, P.Y., H.T. Ma, H.J. Lee, and R.Y.C. Poon. 2016. MASTL(Greatwall) regulates DNA damage responses by coordinating mitotic entry after checkpoint recovery and APC/C activation. *Sci. Rep.* 6:22230. https://doi.org/10.1038/srep22230

Yoon, Y.N., M.H. Choe, K.-Y. Jung, S.-G. Hwang, J.S. Oh, and J.-S. Kim. 2018. MASTL inhibition promotes mitotic catastrophe through PP2A activation to inhibit cancer growth and radioresistance in breast cancer cells. *BMC Cancer.* 18:716. https://doi.org/10.1186/s12885-018-4600-6

Zaidel-Bar, R., R. Milo, Z. Kam, and B. Geiger. 2007. A paxillin tyrosine phosphorylation switch regulates the assembly and form of cell-matrix adhesions. *J. Cell Sci.* 120:137–148. https://doi.org/10.1242/jcs.03314

Zaidel-Bar, R., G. Zhenhuan, and C. Luxenburg. 2015. The contractome--a systems view of actomyosin contractility in non-muscle cells. *J. Cell Sci.* 128:2209–2217. https://doi.org/10.1242/jcs.170068

Downloaded from http://rupress.org/jcb/article-pdf/219/6/e201906204/1615651/jcb_201906204.pdf by guest on 09 February 2026

Supplemental material

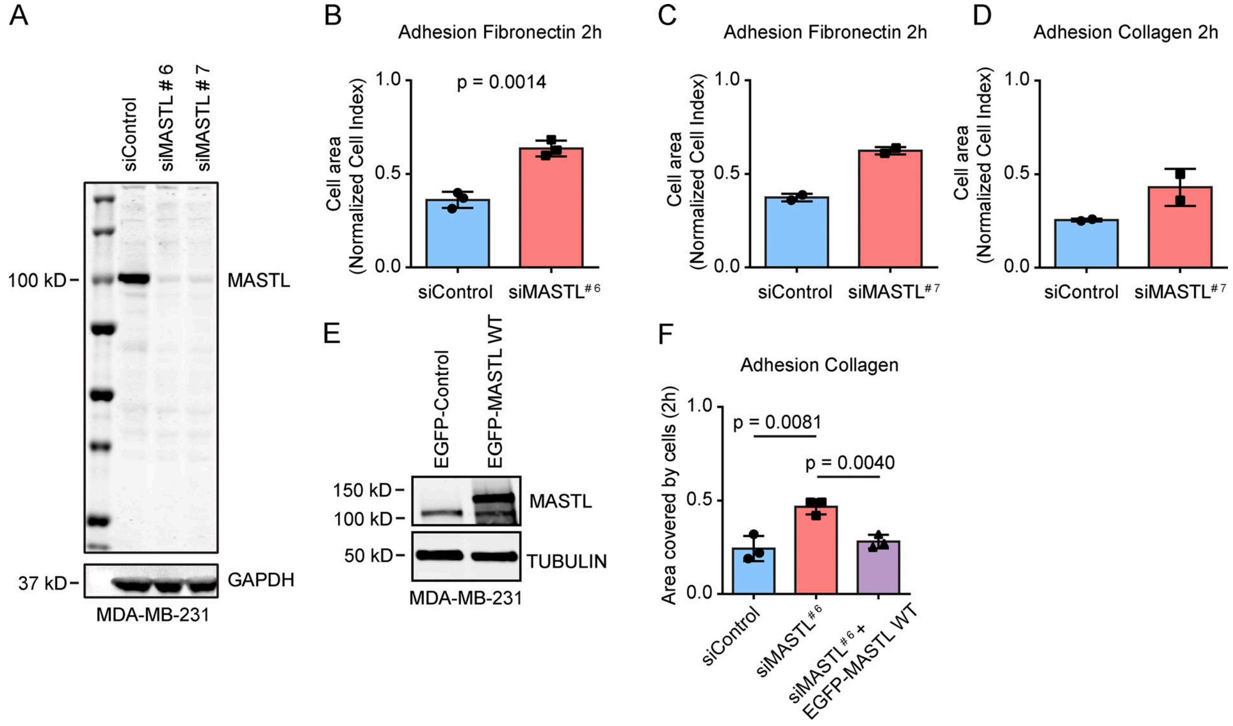

Figure S1. **MASTL inhibits cell spreading and attachment (related to Figure 1). (A)** Western blot analysis of MASTL and GAPDH after MASTL silencing (48 h) with siRNAs #6 and #7 in MDA-MB-231 cells. **(B–D)** Quantification of cell attachment (normalized cell index, impedance) at the 2-h time point measured with xCELLigence after plating of single MDA-MB-231 cells (siControl or siMASTL, 48 h) on fibronectin silenced with siMASTL#6 (*n* = 4 biologically independent experiments, mean ± SD, unpaired *t* test; B), fibronectin silenced with siMASTL#7 (*n* = 2 biologically independent experiments; C), or collagen silenced with siMASTL#7 (*n* = 2 biologically independent experiments; D). **(E)** Western blot analysis of MASTL and tubulin in MDA-MB-231 cells after 24-h overexpression of EGFP-control or EGFP-MASTL WT. **(F)** Quantification of cell attachment at the 2-h time point (from Fig. 1 I curves) of siControl (48 h), siMASTL (48 h), or EGFP-MASTL WT–reexpressing (24 h silencing + 24 h expression of siRNA-resistant MASTL) MDA-MB-231 cells on collagen. See also Table S1.

Downloaded from http://rupress.org/jcb/article-pdf/219/6/e201906204/1615651/jcb_201906204.pdf by guest on 09 February 2026

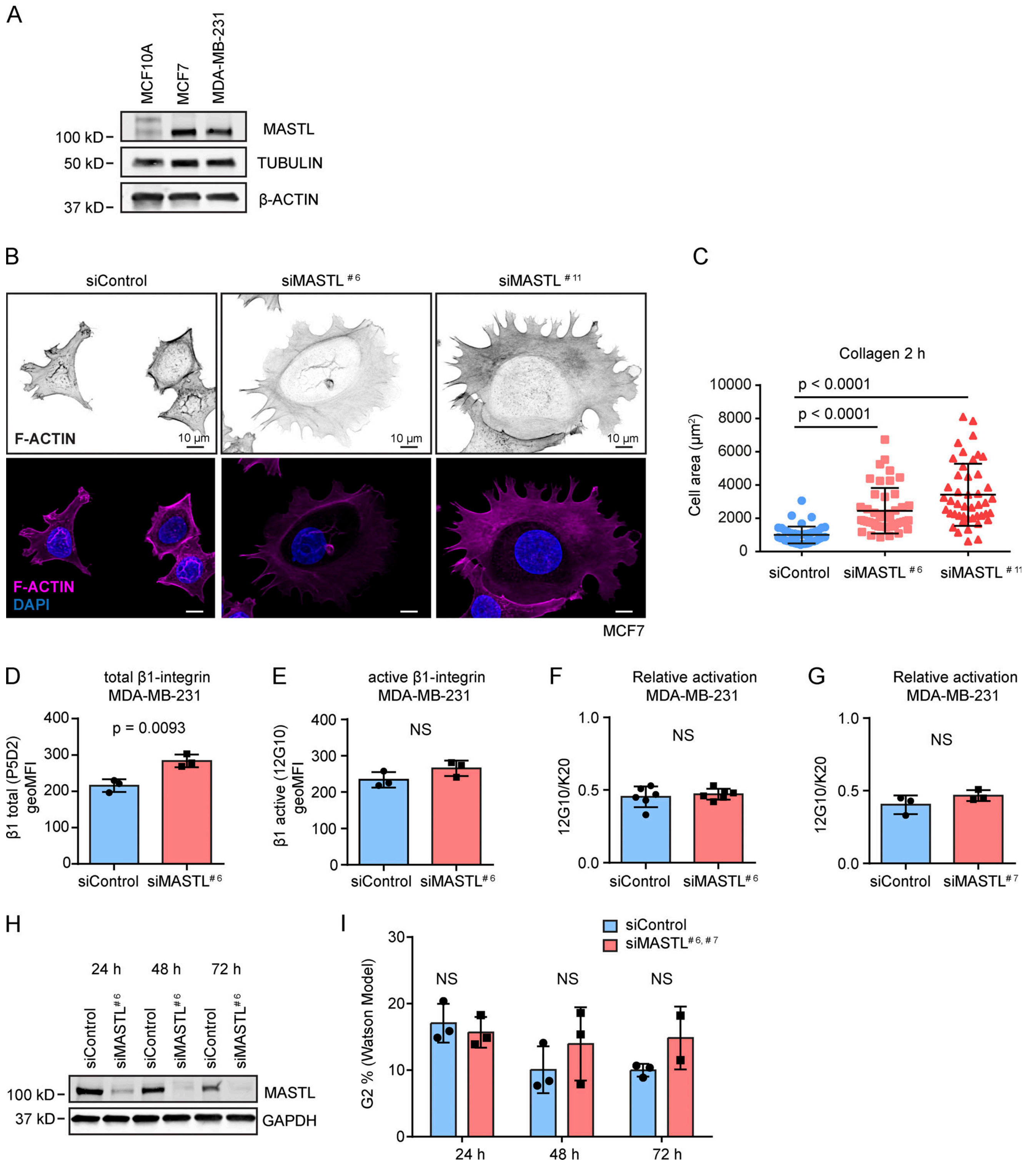

Figure S2. **MASTL regulates cell spreading independently of focal adhesion size, integrin activity or cell cycle (related to Fig. 2). (A)** Western blot analysis of MASTL, tubulin and β-actin in MCF10A, MCF7 and MDA-MB-231 cells. **(B)** Representative images of F-actin (Phalloidin-Atto) and DAPI staining in control (siControl) or MASTL-silenced (siMASTL; 48 h silencing) MCF7 cells plated on collagen for 2 h. Images were acquired on a 3i CSU-W1 spinning disk confocal. **(C)** Quantification of cell area based on F-actin staining of 45 cells (3 independent experiments) from B. **(D and E)** Quantification of the flow cytometry of total β1-integrin (P5D2; D) or active β1-integrin (12G10; E) in siControl and siMASTL (48 h) cells (n = 3 biologically independent experiments, mean ± SD, unpaired t test, MDA-MB-231). **(F and G)** Level of active β1 integrin (12G10) relative to total β1 integrin (K20) after MASTL#6 silencing (F; n = 6 independent experiments, mean ± SD, t test, MDA-MB-231) or after MASTL#7 silencing (G; n = 3 independent experiments, mean ± SD, unpaired t test). **(H)** Western blot analysis of MASTL and GAPDH in siControl and siMASTL (24, 48, or 72 h) MDA-MB-231 cells at different time points. **(I)** Quantification of the flow cytometry data (Fig. 2 I). Proportion of MDA-MB-231 cells in the G2 phase of the cell cycle (Watson model) after silencing of MASTL for 24, 48, and 72 h (n = 3 independent experiments [1 × #6, 2 × #7], mean ± SD, unpaired t test). See also Table S1.

Downloaded from http://rupress.org/jcb/article-pdf/219/6/e201906204/1615651/jcb_201906204.pdf by guest on 09 February 2026

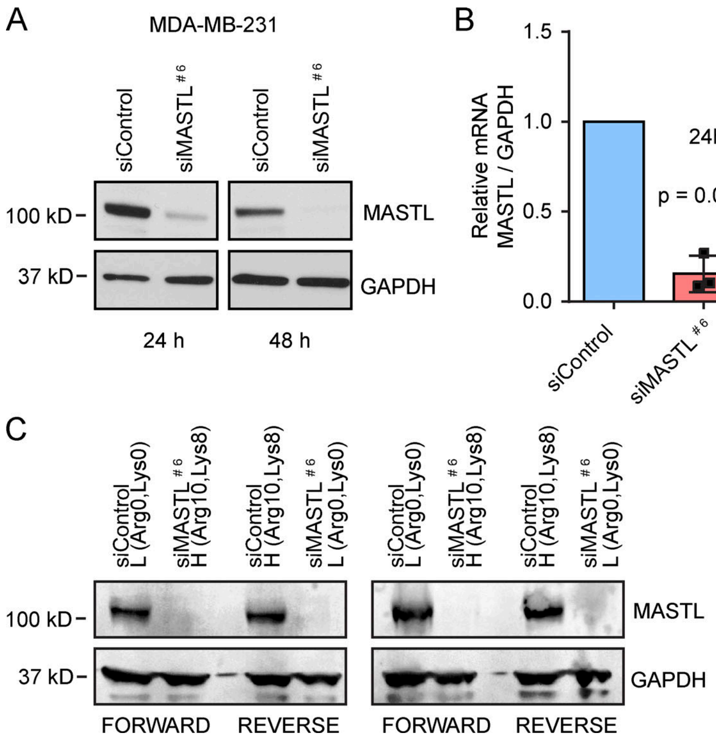

Figure S3. **MASTL silencing confirmed with Western blot and RT-PCR (for experiments related to Fig. 4). (A)** Western blot analysis of MASTL and GAPDH 24 h and 48 h after silencing of MASTL#6 in samples used for the transcriptional analysis, MDA-MB-231 cells. **(B)** RT-PCR of MASTL relative to GAPDH 24 h and 48 h after silencing of MASTL#6 in samples used for the transcriptional analysis (*n* = 3 independent experiments, mean ± SD, unpaired *t* test, MDA-MB-231 cells). **(C)** Western blot analysis of MASTL and GAPDH 48 h after silencing of MASTL#6 in MDA-MB-231–labeled cells used for the total proteome analysis (MDA-MB-231 cells). H, heavy isotopes (Arg10, Lys8); L, light isotopes (Arg0, Lys0). See also Table S1.

Downloaded from http://rupress.org/jcb/article-pdf/219/6/e201906204/1615651/jcb_201906204.pdf by guest on 09 February 2026

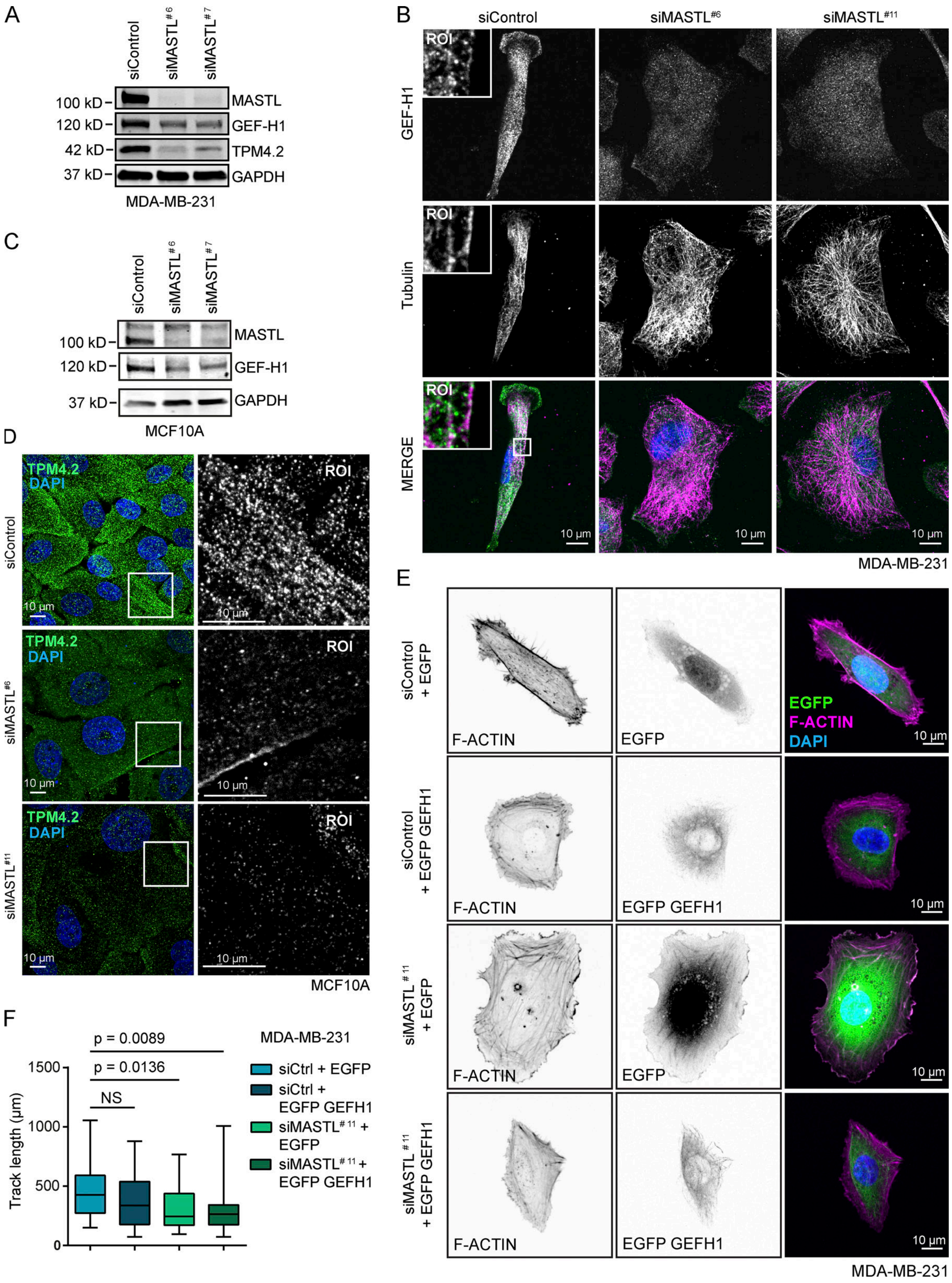

Figure S4. **MASTL regulates GEF-H1, Tpm4.2, and NM-2B levels and GEFH1 rescues cell spreading, but not cell migration, in MASTL-silenced cells (related to Figure 5). (A)** Western blot analysis of GEF-H1, Tpm4.2, and MASTL protein levels in siControl, siMASTL#6, and siMASTL#7 MDA-MB-231 cells. **(B)** Representative GEF-H1 and tubulin staining in siControl, siMASTL#6, and siMASTL#11 MDA-MB-231 cells. Images were acquired on a 3i CSU-W1 spinning disk confocal. **(C)** Western blot analysis of GEF-H1 and MASTL protein levels in siControl, siMASTL#6, and siMASTL#7 MCF10A cells. **(D)** Representative Tpm4.2 staining in siControl, siMASTL#6, and siMASTL#11 MCF10A cells. **(E)** Representative F-actin (Phalloidin-Atto) and DAPI staining in siControl and siMASTL#11 MDA-MB-231 cells transfected with EGFP or EGFP-GEF-H1 for 24 h and plated on collagen for 2 h. Images were acquired on a 3i CSU-W1 spinning disk confocal. **(F)** Migration track length of siControl and siMASTL#11 MDA-MB-231 cells transfected with EGFP or EGFP-GEF-H1 for 24 h. Cells were imaged every 10 min for 600 min in total (*n* = 3 biologically independent experiments, mean ± SD, unpaired *t* test). See also Table S1.

Downloaded from http://rupress.org/jcb/article-pdf/219/6/e201906204/1615651/jcb_201906204.pdf by guest on 09 February 2026

https://doi.org/10.1083/jcb.201906204

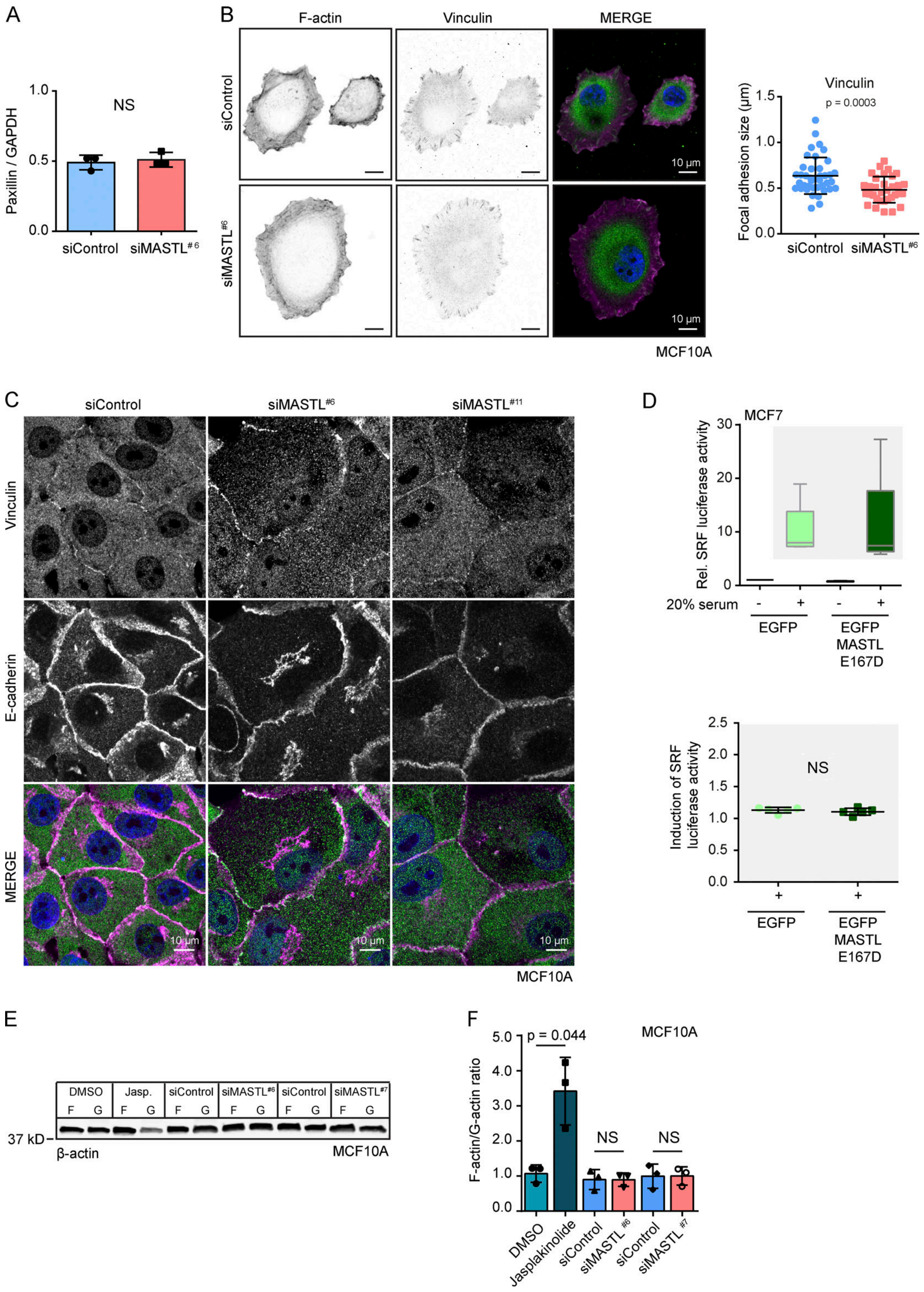

Figure S5. **MASTL regulation of vinculin-positive focal adhesions and SRF activity (related to Fig. 8). (A)** Quantification of paxillin levels after MASTL silencing. Protein levels are normalized by GAPDH (n = 3 biologically independent experiments, mean ± SD, unpaired t test). **(B)** Representative images of F-actin (Phalloidin-Atto), vinculin, and DAPI staining in siControl and siMASTL (48 h silencing) MCF10A cells plated on collagen for 2 h, and quantification of focal adhesion size based on vinculin staining (three independent experiments). Images were acquired on a 3i CSU-W1 spinning disk confocal. **(C)** Representative staining of vinculin and E-cadherin in confluent siControl, siMASTL#6 and siMASTL#11 MCF10A cells. Images were acquired on a 3i CSU-W1 spinning disk confocal. **(D)** Relative SRF luciferase activity. MCF7 cells expressed EGFP control and EGFP-MASTL E167D together with the SRF reporter 3D.Aluc and RLTK Renilla luciferase transfection control under serum-starved conditions and after stimulation with 20% serum. **(E)** Western blot of β-actin in F- and G-actin fractions of MCF10A cells treated with DMSO or jasplakinolide (Jasp.; 0.1 µM, 30 min) or silenced with siControl, siMASTL#6, or siMASTL#7 (48 h). **(F)** Quantification of F-actin protein levels relative to G-actin in MCF10A cells after treatments from B (n = 3 biologically independent experiments, mean ± SD, unpaired t test). See also Table S1.

Downloaded from http://rupress.org/jcb/article-pdf/219/6/e201906204/1615651/jcb_201906204.pdf by guest on 09 February 2026

Video 1. **siControl MDA-MB-231 cells migrating on collagen.** Bright-field time-lapse image sequences taken at 10-min intervals. Video corresponds to Fig. 7 A. Frame rate of the video is 7 frames per second.

Video 2. **siMASTL MDA-MB-231 cells migrating on collagen.** Bright-field time-lapse image sequences taken at 10-min intervals. Video corresponds to Fig. 7 A. Frame rate of the video is 7 frames per second.

Video 3. **Focal adhesion kinetics in mEmerald-paxillin-labelled siControl and siMASTL MDA-MB-231 cells.** Time-lapse image sequences taken at 1-min intervals. Video corresponds to Fig. 7 D. Frame rate of the video is 7 frames per second.

Provided online are three tables. Table S1 contains the statistics related to all figures in an Excel file. Table S2 shows the Illumina transcriptome data of MASTL-silenced cells (related to Fig. 3) in an Excel file. Table S3 contains the SILAC proteome data of MASTL-silenced cells (related to Fig. 3) in an Excel file.

Downloaded from http://rupress.org/jcb/article-pdf/219/6/e201906204/1615651/jcb_201906204.pdf by guest on 09 February 2026